Evaluating the subsidence above gas reservoirs with an elasto-viscoplastic constitutive law. Laboratory evidences and case histories

Date paper revised: September 10th, 2020

To be submitted to

Geomechanics for Energy and the Environment:

Evaluating the subsidence above gas reservoirs with an elasto-viscoplastic constitutive law: laboratory evidences and case histories

G. Musso[a,*], G. Volonté[b], F. Gemelli[c], A. Corradi[c],

S.K. Nguyen[a,d], R. Lancellotta[a], M. Brignoli[c] and S. Mantica[c]

a - Department of Structural, Building and Geotechnical Engineering, Politecnico di Torino, corso Duca degli Abruzzi 24, 10129 Torino, ITALY.

b - Department of Petroleum R&D, Eni S.p.A., Via Maritano 26, 20097 San Donato Milanese, ITALY.

c - Department of EOR Technologies and Geomechanics, Eni S.p.A., Via Emilia 1, 20097 San Donato Milanese, ITALY.

d - Department of Mechanics of Structure and Materials, Institut Supérieur de l'Aéronautique et de l'Espace (ISAE), Avenue Édouard-Belin 10, 31055 Toulouse, FRANCE.

*corresponding author guido.musso@polito.it

Abstract

Reliable modelling of subsidence is an important objective for companies and regulators interested in safe and environmentally sustainable development of hydrocarbon fields. Subsidence is triggered by the depletion of reservoirs and connected aquifers, which causes the compaction of the geologic layers. A fundamental requirement of models is the correct prediction of the pore pressure changes taking place during the production; but capturing the mechanical behaviour of the reservoir material and its proper constitutive modelling are equally important. In some cases, the geologic materials show a time-dependent (viscous) behaviour, which might lead to creep strains at constant stress conditions. As a consequence, subsidence might be delayed with respect to hydrocarbon production, or continue even when production has stopped.

This paper refers to the case of two gas reservoirs from the Adriatic basin. Numerical simulations based on elasto-plastic constitutive models, even if relying on very accurate reconstructions of the pore pressure histories, did not provide a satisfactory match of subsidence history. This motivated a further insight into the time-dependent behaviour of the sandy reservoir materials. The results of an exhaustive laboratory investigation were interpreted in light of an existing elasto-viscoplastic model, recently implemented by the authors in a commercial Finite Element code. Numerical predictions are compared to field data, which include both measurements of compaction, taken in the reservoirs with radioactive markers, and surface settlements recorded with GPS and bathymetric surveys. A very good agreement was obtained between simulation results and field data, in terms of maximum settlements, settlement history and extent of the subsidence bowl.

Keywords:

Subsidence; time-dependent mechanical behaviour; creep; elasto-viscoplastic constitutive law; gas reservoir; case history

1. Introduction

Land subsidence is a potential undesired effect of underground fluid extraction, which in some cases can seriously affect the environment and human activities. Subsidence can increase the risk of flooding along coastal and estuarine areas, as in New Orleans with the Katrina Hurricane[1] and in Bangkok in 2011[2]. In extreme cases, anthropic subsidence can cause the ground floor to sink below the water level, which in proximity of populated or environmentally relevant lands can impact on social or ecological equilibria[3], requiring the building of new dykes (see e.g. Refs. 4, 5) or rising the height of old ones[6]. In offshore fields, subsidence due to hydrocarbon extraction can reduce the air gap between the lower platforms deck and the sea, exposing platforms to waves inundation and requiring very costly extraordinary maintenance to keep the production activities ongoing[7]. Both regulators and energy companies are then deeply interested in reliable predictive models, which allow foreseeing the magnitude and extent of the ground settlements, ultimately leading to early implementation of mitigation strategies whenever necessary.

Factors that can lead to appreciable subsidence are highly compressible reservoir rocks, considerable decrease of pore pressure during hydrocarbon production, thick or shallow reservoirs and low contrast between the stiffness of the reservoir and that of the overburden[8].

Saturated soils and rocks have a coupled hydro-mechanical behaviour and, in principle, both the flow and the mechanical problems should be solved simultaneously through coupled hydro-mechanical analyses. This is seldom done, because of the demanding numerical issues and computational efforts required for large scale problems such as the one under consideration (e.g. Ref. 9). However, for gas reservoirs, very little hydro-mechanical coupling is expected because the pore fluid has a very high compressibility compared to the rock. A one-way coupling procedure, where the pore pressure distribution at different times is first estimated by means of reservoir fluid dynamic simulations and then used to simulate the mechanical response, is accepted in these cases, provided that the mechanical characterization of reservoir rocks is consistent in both flow and mechanical models. The first mathematical model for the prediction of subsidence was formulated by Geertsma[10] on the basis of the 'strain nuclei' approach. This model considers the subsurface as a poro-elastic half space, and it provides the analytical solution of the displacement caused by the pore pressure drop occurring within a material point (nucleus of strain) having some specific coordinates. The analytical solution can be readily extended to real cases by discretizing the reservoir with a proper number of grid blocks (strain nuclei) and integrating the effects of the pressure decrease of each grid block over the whole reservoir, thus predicting the subsidence bowl due to the development of the field. The solution for the simplified case of an axisymmetric disc-shaped reservoir with a uniform pressure can be found in Geertsma[11].

The Geertsma model introduces the very stringent assumptions of a homogeneous material with a linear isotropic elastic behaviour. Other analytical models (see e.g. Refs. 12, 13) relaxed the homogeneity and the isotropy assumptions, while maintaining linear elasticity. However, it is well known that the mechanical behaviour of most of the geologic materials is elastic only at very small strains, and that it is generally not linear.

A significant improvement in subsidence modelling was obtained accounting for plastic strains occurring along compression stress paths, by implementing volumetric hardening elasto-plastic models such as the Modified Cam Clay Model[14] into Finite Element (FE) codes. Simulations based on these models proved to be satisfactory for several field cases[15-17], but failed in detecting the correct values and trends of subsidence for others[18-21], where an increase in subsidence was appreciated even after production had stopped or reduced significantly.

Two major mechanisms are considered to be responsible for the delayed subsidence and for the discrepancy between the simulations and field measurements. The first one is the delayed depletion of low permeability layers, such as shales or clays, both within and outside the reservoir (see e.g. Ref. 22). Pore pressure decrease, originating in the gas bearing layers, diffuses very slowly through shales or clays, because of their low permeability. As such, shale compaction will continue after suspending or even stopping production. Such a compaction adds up to the one of the reservoir and induces a delayed increase of subsidence, which can be observed only in later stages of the productive life of the field. However, delayed subsidence has been observed also in the first years of production, without any relationship to stop of production[23].

Delayed subsidence might also depend on the time-dependent behaviour of the materials. For soils, volume strains are well known to increase with time even under a constant effective stress, a creep phenomenon known as secondary compression[24,25]. A similar behaviour has been observed with reservoir sands[26] and shales[27] loaded to high effective stresses. Chang et al.[20] studied the subsidence history of onshore gas fields by summing the elastic subsidence of a disc-shaped reservoir (evaluated according to Geertsma[11]) to the compaction of the shale layers surrounding the reservoir. The hydraulic behaviour of the shales was modelled with the one-dimensional diffusion equation whereas the mechanical behaviour was modelled with a one-dimensional viscoplastic law. Notwithstanding the simplifying assumptions, introduced both with respect to the geometry and the hydro-mechanical behaviour, they obtained a good qualitative match of the subsidence history, suggesting that creep and delayed depressurization of shales are key aspects to be taken into account for the improvement of subsidence predictions (see also Ref. 28).

This paper aims at discussing the impact of the time-dependent behaviour of reservoir sands on the subsidence of gas fields. After briefly introducing some elasto-viscoplastic models of use for soils and rocks, the main results of a laboratory investigation on the time-dependent behaviour of sands from two reservoirs of the Adriatic basin are provided. The

adequacy of the elasto-viscoplastic model of Vermeer and Neher[29] (VNM in the following) in reproducing the laboratory results is discussed, justifying its implementation into a commercial FE code. Laboratory tests served also to determine the VNM parameters to be used for the numerical simulations of the subsidence of the two fields. The pressure history and related compaction of clay layers were taken into account in the simulations where appropriate. Model predictions are finally compared to real field data, based upon the extensive subsidence and compaction monitoring campaigns performed.

2. Elasto-viscoplastic models for soils and reservoir rocks

Several models have been formulated in past years to reproduce the time-dependent behaviour of soils and rocks (see e.g. Ref. 30) and both viscoelastic and viscoplastic relationships have been proposed. Elasto-plastic laws with volumetric hardening are currently used by the oil industry for geomechanical simulations. Elasto-viscoplastic models can be seen as an enhancement of elasto-plastic ones. It is then of interest to check their performance in subsidence prediction, since they might ensure an improvement in the cases where the ones obtained using elasto-plasticity are not accurate enough.

A brief description of the families of constitutive models which enhance hardening plasticity to account for time-dependent behaviour, with special reference to elasto-viscoplastic models with volumetric hardening, is given below. These models share the assumption that the total strain can be decomposed into the sum of an elastic and of a viscoplastic component:

$$\boldsymbol{\varepsilon} = \boldsymbol{\varepsilon}^{e} + \boldsymbol{\varepsilon}^{vp} \tag{1}$$

where $\boldsymbol{\varepsilon}$ is the small strain tensor, while $\boldsymbol{\varepsilon}^{e}$ and $\boldsymbol{\varepsilon}^{vp}$ are its elastic and viscoplastic components.

The elastic strains are time independent and they are related to stress increments through some generalized Hooke's law. Viscoplastic strains are time-dependent, and they are usually evaluated either in the frame of the theory of the Non Stationary Flow Surface (NSFS) or in the frame of the Overstress Theory.

2.1 Models formulated in the frame of the Non Stationary Flow Surface

The theory of the Non Stationary Flow Surface has been originally developed by Naghdi and Murch[31] and by Olszak and Perzyna[32] and it is based on the assumption that the yield surface evolves with time, even when the stress is constant.

In volumetric hardening plasticity, the yield function has the expression:

$$f = f\left(\boldsymbol{\sigma}', p'_c(\boldsymbol{\varepsilon}^p, \gamma)\right) \quad (2)$$

where $\boldsymbol{\sigma}$' is the effective stress tensor and p'_c is the hardening parameter, related to the plastic strain tensor $\boldsymbol{\varepsilon}^p$ and, where required, to other variables γ accounting for effects such as grain bonding, saturation, temperature, chemical composition of the pore fluid, etc. In the NSFS models, the yield function depends on the same variables used in elastic-hardening models, but it also depends on some time-dependent function β:

$$f = f\left(\boldsymbol{\sigma}', p'_c(\boldsymbol{\varepsilon}^{vp}, \gamma), \beta\right) \quad (3)$$

The effect of time is often introduced through the viscoplastic strain rate $\dot{\boldsymbol{\varepsilon}}^{vp}$ and specifically imposing that the hardening parameter depends both on the viscoplastic strain and on the viscoplastic strain rate:

$$p'_c = p'_c(\boldsymbol{\varepsilon}^{vp}, \dot{\boldsymbol{\varepsilon}}^{vp}, \gamma) \quad (4)$$

Equation 4 is consistent with the isotach concept proposed by Šuklje[33], which states that the state of a volume of soil can be described by a single $(p', e, \dot{e})$ relationship, where p' is the mean effective stress, e and $\dot{e}$ are the void ratio and the rate at which it changes. Under the hypothesis of incompressible solid grains, the volume strain is

$$\varepsilon_v = -\frac{\Delta e}{1+e_0} \quad (5)$$

where Δe is the change in void ratio and e_0 is the void ratio at some reference conditions. The isotach concept implies then that the position of the Normal Compression Line (describing first time compression of the soil volume) in the compression plane (p', e) depends on the applied strain rate: first time compressions at different strain rates are described by different Normal Compression Lines. During a creep phase, the stress remains constant and the strains increase but their velocity decreases with time. Therefore, as remarked by De Gennaro and Pereira[34] "soils may experience both compression under constant strain rate (i.e. following a rate-line) or delayed compression under sustained constant load (i.e. decreasing the strain rate and crossing multiple rate-lines)" (see Fig. 1). The yield stress increases then with the strain rate (see e.g. Ref. 35).

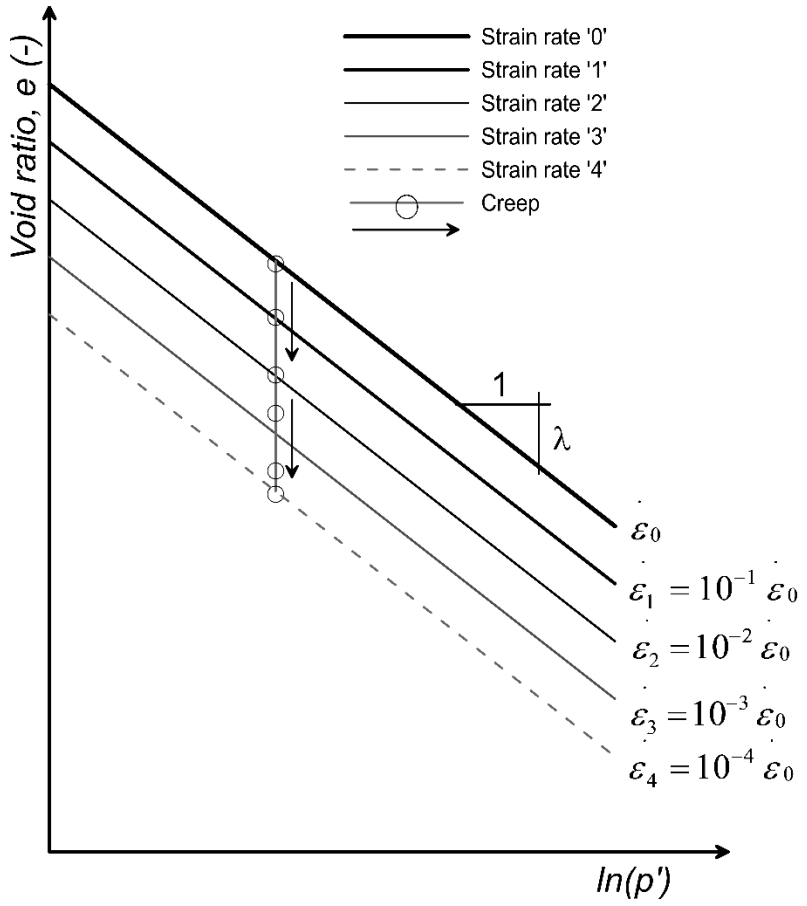

Fig. 1. Isotach concept: Normal Compression Lines at different constant strain rates are parallel lines on the compression plane. During a creep process the stress remains constant while the volume decreases at decreasing rates, thus crossing the NCL of different strain rates

de Waal and Smits[36] presented results of one-dimensional compression of sandstones, interpreted with a stress rate dependent model, which have been also reproduced with a strain rate NSFS model by Cassiani et al.[37]. By introducing the assumptions of eq. (4) into eq. (3), it follows:

$$f = f(\boldsymbol{\sigma}', p'_c(\boldsymbol{\varepsilon}^{vp}, \dot{\boldsymbol{\varepsilon}}^{vp}, \gamma\ )\ ) \tag{6}$$

The yield function *f* of the Modified Cam Clay Model:

$$f = q^2 - M^2 p'(p'_c - p') \tag{7}$$

is usually adopted (see e.g. Refs 37-38). In (7) q is the deviatoric stress and M the slope of the critical state line in the p',q plane:

$$p' = \frac{1}{3}\sigma'_{ii}, \quad q = \sqrt{3}\sqrt{J_2}, \qquad J_2 = \frac{1}{2}s_{ij}s_{ij} \qquad s_{ij} = \sigma'_{ij} - p'\delta_{ij} \quad M = \frac{6sin\phi'_{cv}}{3-sin\phi'_{cv}} \tag{8}$$

with ϕ'_{cv} friction angle at constant volume conditions.

A NSFS model for unsaturated conditions, relying of the yield and plastic potential functions of the Barcelona Basic Model[39], is discussed in Ref. 34.

The infinitesimal increment of viscoplastic strains $d\boldsymbol{\varepsilon}^{vp}$ is given by:

$$d\boldsymbol{\varepsilon}^{vp} = \Lambda \frac{\partial g}{\partial \boldsymbol{\sigma}'} \tag{9}$$

where g is the plastic potential function and Λ the plastic multiplier. As in hardening plasticity, the stress state is not allowed outside of the yield surface and the constraint $f \leq 0$ applies. Very often an associated flow rule is assumed and $f = g$.

The value of Λ is then determined by introducing eq. (9) into the consistency condition $df = 0$:

$$df = \frac{\partial f}{\partial \boldsymbol{\sigma}'} : d\boldsymbol{\sigma}' + \frac{\partial f}{\partial \alpha} d\alpha + \frac{\partial f}{\partial p'_c}\left(\frac{\partial p'_c}{\partial \varepsilon_v^{vp}} d\varepsilon_v^{vp} + \frac{\partial p'_c}{\partial \dot{\varepsilon}_v} d\dot{\varepsilon}_v\right) = 0 \tag{10}$$

In eq. (10), the two hardening mechanisms are made evident. The first one is related to the magnitude of the viscoplastic volume strain, and it is usually assumed to be the same of the Modified Cam Clay Model:

$$\frac{\partial p'_c}{\partial \varepsilon_v^{vp}} = \frac{1+e_0}{\lambda-\kappa} p'_c \tag{11}$$

where λ is the elasto-viscoplastic logarithmic compliance and κ is the elastic logarithmic compliance, defined in terms of void ratio. The second hardening mechanism is related to the strain rate, which is usually expressed by a power law relating p'_c to $\dot{\varepsilon}_v$.

2.2 Models formulated in the frame of the Overstress Theory

The Overstress Theory was originally developed by Malvern[40] for one-dimensional conditions and extended to the three-dimensional case by Perzyna[41,42] and Olszak and Perzyna [32]. It requires a static yield surface f_s , which separates the non-viscous regime from the viscoplastic regime, thus defining the size of the purely elastic domain, and a dynamic loading surface f_d, related to the current stress state. The Overstress Theory aims at predicting the strain rates, decomposed into elastic and viscoplastic components:

$$\dot{\boldsymbol{\varepsilon}} = \dot{\boldsymbol{\varepsilon}}^e + \dot{\boldsymbol{\varepsilon}}^{vp} \tag{12}$$

The stress state can be within, on, or outside the static yield surface f_s and the consistency condition does not apply. The viscoplastic strain rate $\dot{\boldsymbol{\varepsilon}}^{vp}$ is then given by a flow rule with respect to the dynamic loading surface f_d:

$$\dot{\boldsymbol{\varepsilon}}^{vp} = \mu\langle\phi(F)\rangle\frac{\partial f_d}{\partial \boldsymbol{\sigma}'} \tag{13}$$

where μ is a fluidity parameter and ϕ(F) is the overstress function, expressing the distance between f_d and f_s. According to the original Overstress Theory:

$$\langle\phi(F)\rangle = \begin{cases} 0 & if \quad F \leq 0 \\ \phi(F) & if \quad F > 0 \end{cases} \tag{14}$$

with F > 0, F<0, and F =0 when the state of stress *P* is outside, within, or on f_s[30].

Determination of the static yield surface is problematic: experimental studies generally remarked the dependency of the yield stress on the strain (or loading) rate, but there are no experimental data proving the existence of a threshold rate below which the yield surface does not depend on the rate anymore[43]. To overcome this issue, recent models ('Extended Overstress Theory') adopt a reference yield surface f_r (Fig. 2) instead of the static yield surface f_s, and viscoplastic strains are anticipated also for F< 0[29,44-46]. Equation (12) is then replaced by expressions such as[41]:

$$\dot{\boldsymbol{\varepsilon}}^{vp} = \mu\left\langle\left(\frac{p'^{d}_{c}}{p'^{r}_{c}}\right)^{N}\right\rangle\frac{\partial f_d}{\partial \boldsymbol{\sigma}'} \tag{15}$$

where $\left(\frac{p'^{d}_{c}}{p'^{r}_{c}}\right)$ is the ratio the of intecepts of the two yield surfaces with the *p'* axis and *N* is a material parameter, or a combination of material parameters. As it can be appreciated through eq. 15, the reference yield surface is associated to a reference strain rate.

The size of the reference yield surface, and therefore the value of p'^{r}_{c}, only depends on the viscoplastic strains. Accordingly, the evolution of p'^{r}_{c} is governed by the hardening rule of the reference hardening plasticity model , which is usually given by an expression such as eq. (11).

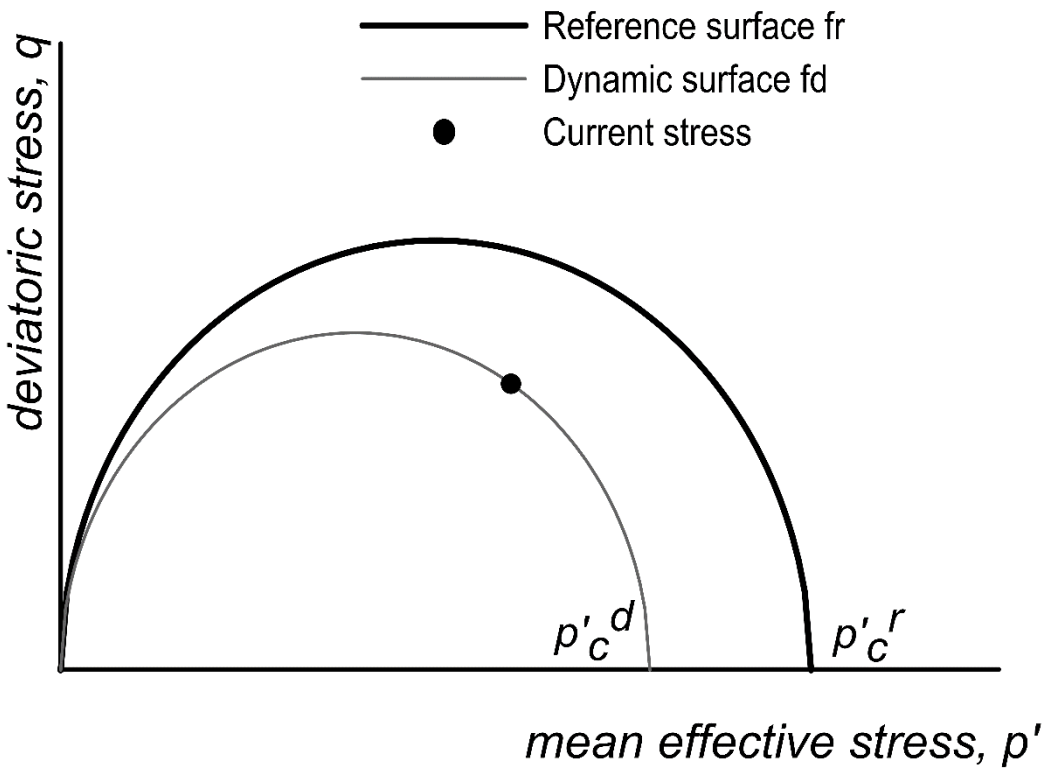

Fig. 2. Dynamic and reference surfaces. Depending on the current stress state, the dynamic surface can either be smaller or bigger than the reference surface.

2.3 Vermeer and Neher Model

'Creep models'are models of the Extended Overstress Theory built on experimental evidences gathered at constant effective stress (creep tests)[43]. The isotropic models described in Refs. 29 and 44 and the anisotropic model of Leoni et al.[47] are all 'creep models'. The formulation of the VNM[29] takes advantage of the results of standard oedometer tests, where the axial stress is increased stepwise and maintained constant for at least 24 hours. In such conditions, after pore pressure dissipation and consolidation, a creep phase takes place. When the applied stress is high enough, the viscoplastic strains grow linearly with the logarithm of time, and a creep index μ^* can be defined as:

$$\mu^* = \frac{\Delta\varepsilon_v^{vp}}{\Delta ln(t)} \tag{16}$$

where $\Delta\varepsilon_v^{vp}$ is the increase in the viscoplastic volume strain and t is time. By writing the viscoplastic volume strain at time τ = 24 hours as $\bar{\varepsilon}_v^{vp}$, it follows:

$$\mu^* = \frac{\varepsilon_v^{vp} - \bar{\varepsilon}_v^{vp}}{ln(t) - ln(\tau)} \quad (17)$$

so the relationship between time and viscoplastic strain is:

$$\frac{t}{\tau} = exp\left(\frac{\varepsilon_v^{vp} - \bar{\varepsilon}_v^{vp}}{\mu^*}\right) \quad (18)$$

The viscoplastic volumetric strain rate is then:

$$\dot{\varepsilon}_v^{vp} = \frac{\mu^*}{\tau} exp\left(\frac{\varepsilon_v^{vp} - \bar{\varepsilon}_v^{vp}}{\mu^*}\right) \quad (19)$$

In the VNM, the reference yield function f_r describes the state of the material which has been loaded for the reference time τ. However, in light of eq. 18, it is also related to a constant strain rate $\dot{\varepsilon}_v^{vp} = \frac{\mu^*}{\tau}$.

The viscoplastic volume strains occurring during a creep phase induce hardening, *i.e.* the hardening parameter $p'_c{}^r$ evolves, with $p'_c{}^r = p'_c{}^d$ when $t = \tau$ and $p'_c{}^r > p'_c{}^d$ when $t > \tau$. Adopting the hardening rule of the Modified Cam Clay:

$$\varepsilon_v^{vp} - \bar{\varepsilon}_v^{vp} = (\lambda^* - \kappa^*) ln\left(\frac{p'^r_c}{p'^d_c}\right) \quad (20)$$

with $\lambda^* = \frac{\lambda}{1+e}$ and $\kappa^* = \frac{\kappa}{1+e}$. By introducing eq (20) into eq. (19) the volumetric viscoplastic strain rate can be related to the ratio between the dynamic and the reference surfaces:

$$\dot{\varepsilon}_v^{vp} = \frac{\mu^*}{\tau}\left(\frac{p'^d_c}{p'^r_c}\right)^{\frac{\lambda^* - \kappa^*}{\mu^*}} \quad (21)$$

Consistency between eq.(15) and eq.(21) implies $N = \frac{\lambda^* - \kappa^*}{\mu^*}$ and $\mu = \frac{\mu^*}{\tau \frac{\partial f}{\partial p'}}$ and the substitution that follows into eq. (15) provides the full viscoplastic strain rate tensor for the VNM.

Eq. (21) predicts that any loading process occurring at a certain constant strain rate is characterized by a fixed $\left(\frac{\mathbf{p'^d_c}}{\mathbf{p'^r_c}}\right)$ ratio. Therefore Normal Compression Lines at different strain rates are expected to be parallel lines, and also the VNM is consistent with the isotach concept. The reference yield function f_r describes then the combination of stress states for which a Normal Consolidated type of behaviour applies whenever the load increments are imposed every 24 hours. The $\left(\frac{\mathbf{p'^d_c}}{\mathbf{p'^r_c}}\right)$ ratio is a measure of the 'distance' from this state, and its inverse can be used to define an apparent Over Consolidation Ratio (OCR). Differently from elasto-plastic models, the apparent OCR does not depend only on the

loading sequence and then on the maximum stress that had been applied. For instance, during a prolonged creep phase, the OCR grows since $p'_c{}^d$ remains constant while $p'_c{}^r$ increases with the accumulated viscoplastic strains, in virtue of the hardening rule (eq (11)).

3. Experimental behaviour of clastic materials from the Adriatic basin and comparison with VNM predictions

A previous experimental characterization of the time-dependent behaviour of clastic materials from the Adriatic basin has been described in Ref. 48. Sandy and clayey samples were loaded in the oedometer until reaching some stress higher than the *in-situ* one, which was mantained constant for 2 weeks. Creep strains were appreciated, while when resumpting the monotonic loading the compressibility of these samples was initially smaller than the one of analogous samples that had not been exposed to creep. At higher stresses,the behaviour of the two types of samples was comparable again. Some preliminary data suggested that the stress range over which the compressibility is reduced because of creep depends on the OCR and on the duration of creep. The OCR also impacted on the creep rate. These evidences are similar to the ones found for various soils or rocks (e.g. Refs. 35,36,49-53) and confirm that Adriatic sediments show appreciable viscoplastic effects, such as those that might be taken into account by the VNM through the hardening law relating the yield stress to the viscoplastic volume strains.

The present work, based on the results of a new comprehensive set of experimental tests, is aimed at:

- gaining a further insight on the mechanical behaviour of the Adriatic offshore sediments, accounting for different loading histories and creep times;
- comparing the experimental findings with the results of simulations based on the VNM model;
- defining robust experimental protocols for the determination of the model parameters;
- providing the parameters for subsidence simulations for the fields of concern.

3.1 Materials

The experimental study was performed on clastic samples from the reservoirs of two fields (for confidentiality reasons defined as Field 1 and Field 2 in the following), focusing on the evaluation of the viscoplastic behaviour. The grain size distribution, obtained through laser diffractometry, and the related classifications are provided in Fig. 3 and Table 1. While all the samples from the Field 1 reservoir were classified as silty sand and have about the same grain size

distribution, the samples from the Field 2 reservoir fall into two classes, one being a clayey silt and the other being a silty sand.

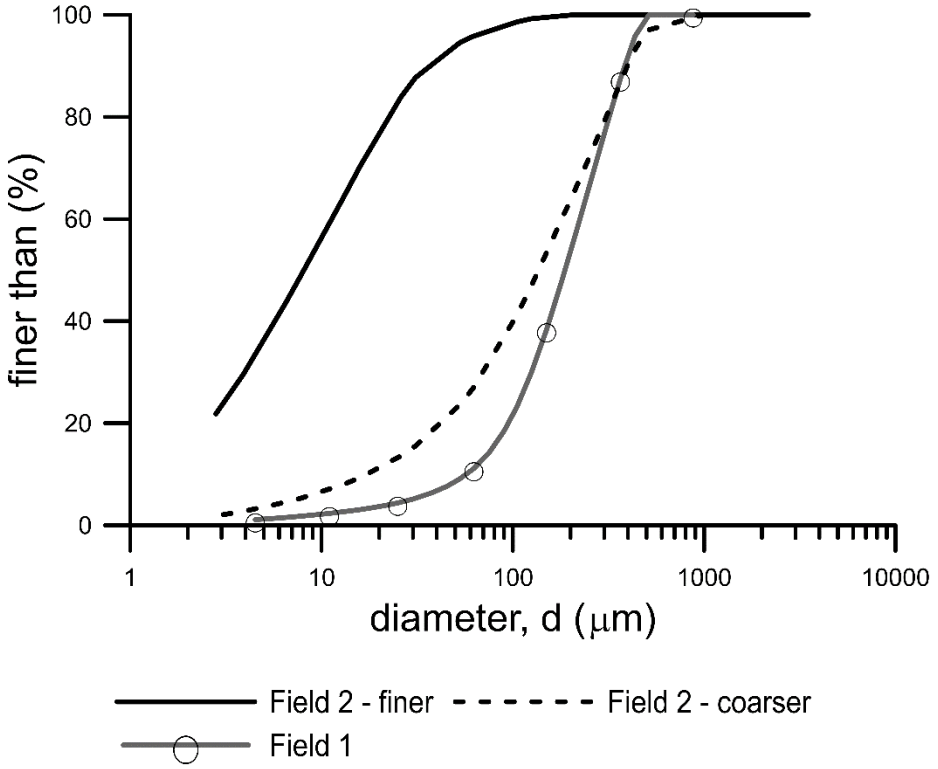

Fig. 3. Grain size distributions of studied samples

Table 1

Grain size fractions according to British standard 5930.

	Clay (d < 2 μm)	Silt (2 μm ≤ d < 60 μm)	Sand (60 μm ≤ d < 2 mm)
Field 1	1	10	89
Field 2 (finer)	22	74	4
Field 2 (coarser)	2	25	73

3.2 Testing protocols

Samples were water saturated and tested under oedometer conditions. For each material, three different multistage step Loading Sequences (LS) were adopted (Fig. 4):

LS 1: the axial stress σ_a was increased every 24 hours as in 'conventional' oedometric tests. No prolonged creep phases were imposed. A comparison of the results of this procedure with other sequences was made, to verify the possibility of determining the parameters of the VNM with relatively quick, standard procedures;

LS 2: the axial stress σ_a was increased every 24 hours up to a value higher than the geostastic one (equal to 10.2 MPa for Field 1 and 9.3 MPa for Field 2). σ_a was then kept constant for two weeks to induce a well developed secondary compression. The stress increments which followed were applied in small steps to appreciate possible hardening due to creep, detected as an increase of the apparent preconsolidation stress;

LS 3: the axial stress was first increased every 24 hours up to σ_a = 8 MPa, a stress which is smaller than the geostratic one for all samples, where a first creep phase of two weeks was imposed. They were then further loaded up to 16 MPa with increments of 2 MPa imparted every 24 hours, and unloaded back to 8 MPa with the same progression. The axial stress was then increased to σ_a = 10 MPa and a second creep phase of two weeks was imposed. A final loading – unloading cycle up to 58 MPa applying the load increments every 24 hours was then imposed. This loading sequence was aimed at checking the relevance of creep from Over Consolidated states. Since the loading history is an important information for proper modelling with the VNM, the loading – unloading sequence imposed before the creep stage at σ_a = 10 MPa was chosen to make at least the recent history available for modelling.

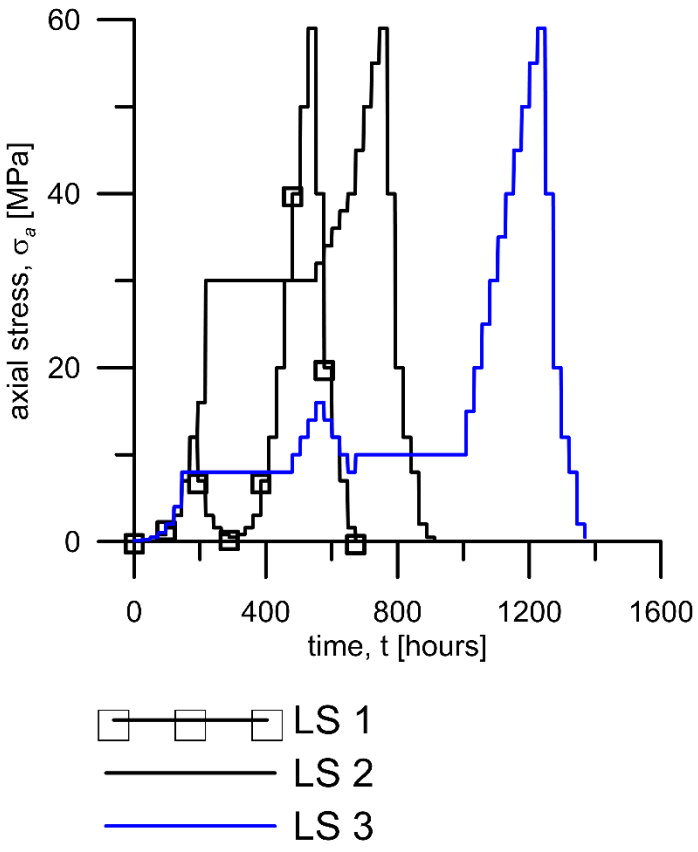

Fig. 4. Loading sequence adopted in the multistage oedometer loading tests

Constant strain rate triaxial with null lateral strain tests (CRS-K_0) previously performed on dry Field 1 samples[54] were also reinterpreted. In these tests, the axial stress was first increased at a constant strain rate up to σ_a = 15 MPa, and it was then kept constant while recording the creep strains. Subsequently, loading and unloading were applied by imposing again constant strain rates.

3.3 Experimental results and model predictions

This section presents the results of laboratory tests together with the predictions of the numerical modelling performed using the VNM model. The same type of mechanical response was obtained with all the materials and the discussion is here limited to the Field 2 samples. In the simulations the specimens were treated as a reference elementary volume, eq. (15) was discretized in time and solved numerically with the software Matlab®. The numerical implementation was done accounting for the constraints of null radial and circumferential strains which hold in oedometer conditions. In the LS tests the axial stress was increased by steps and the saturated samples also experienced mechanical consolidation, which according to the interpretation in the frame of the Terzaghi's one-dimensional equation occured within 10 minutes from each load increase. Consistently, the experimental creep strains, labeled as ε_a^* in the following, are determined as the difference between the current axial strain ε_a and the axial strain at the end of consolidation, *i.e.* 10 minutes after imposing the load. In the numerical analyses the consolidation process was approximated by adopting load ramps of 10 minutes.

Fig. 5a shows the experimental stress-strain curve and the model predictions for the LS1 test. The figure provides the axial strain ε_a at the end of the consolidation and 24 hours from loading for each step. The model reproduces quite well the experimental results, in particular for stresses higher than about 12 MPa and along the unloading – reloading sequence. Fig. 5b provides the time history of the creep strains ε^*_a for selected stresses. ε_a^* increases about linearly with the logarithm of time, with a rate that at first increases with the stress and becomes about constant for $\sigma'_a \geq$ 30 MPa. The slope of ε_a^* vs. ln(t) at high stresses was used to evaluate the μ^* parameter of the VNM, while the slopes of the loading and of the unloading – reloading lines, defined for the 24 hours strains $\bar{\varepsilon}_a$, were used to determine λ^* and κ^*, respectively. The dependency of the experimental strain rate on the stress is in agreement with the predictions of the VNM model. According to eq. (21), the strain rate grows with the p'^d_c/p'^r_c ratio. At lower stresses the specimen is overconsolidated and this ratio is surely smaller than one, which justifies small strain rates. At high stresses the $\left(\frac{p'^d_c}{p'^r_c}\right)$ ratio at 24 hours is equal to one which justifies identical strain rates for each step.

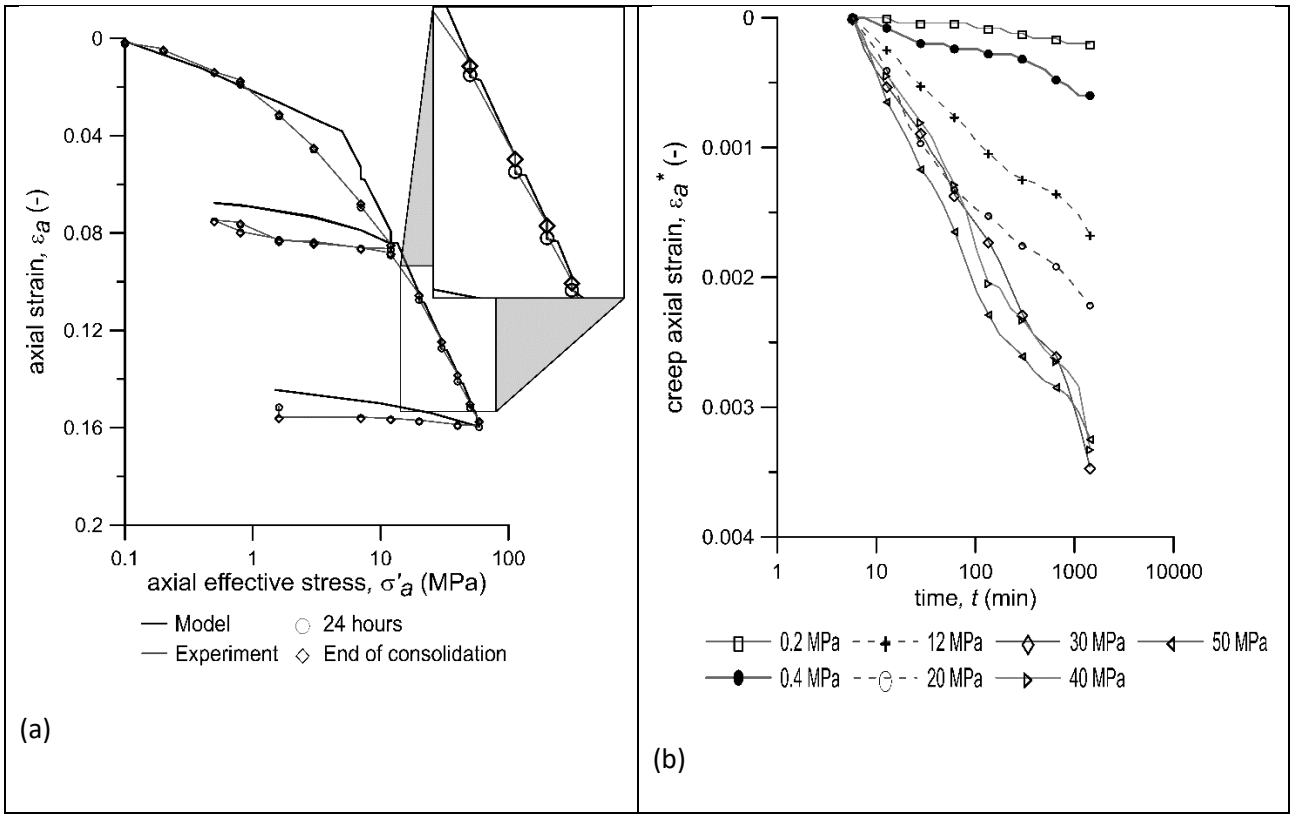

Fig. 5. LS1 test on coarse Field 2 sample. a) stress – strain curves. b) creep strains vs. time

The impact of 14 days of creep, such as the one occurring when σ_a = 30 MPa in the LS2 tests, is shown in Fig. 6. Besides causing larger axial strains, the long creep phase impacts on the behaviour in two ways, which become clear when the axial stress is furtherly increased. For one, the material is stiffer than before. For another, the creep strains accumulating during 24 hours in the following load steps are reduced with respect to the ones occurring at the stresses which preceed the long creep stage. In Fig. 6, the 24 hours creep strains are appreciated as the vertical distance between empty and grey circles. The dashed line provides the position of the Normal Compression Line under oedometer conditions for the 24 hours strain, which gives the relationship between the axial stress on the reference surface and ε_a. After the 14 days creep, the state of the specimen plots to the left of the NCL, justifying an apparent overconsolidation effect and the stiffer behaviour. However, under very high stresses ($\sigma'_a \geq 45$ MPa) the experimental points align again very well with the NCL and the creep strains attained during 24 hours are comparable with the initial ones.

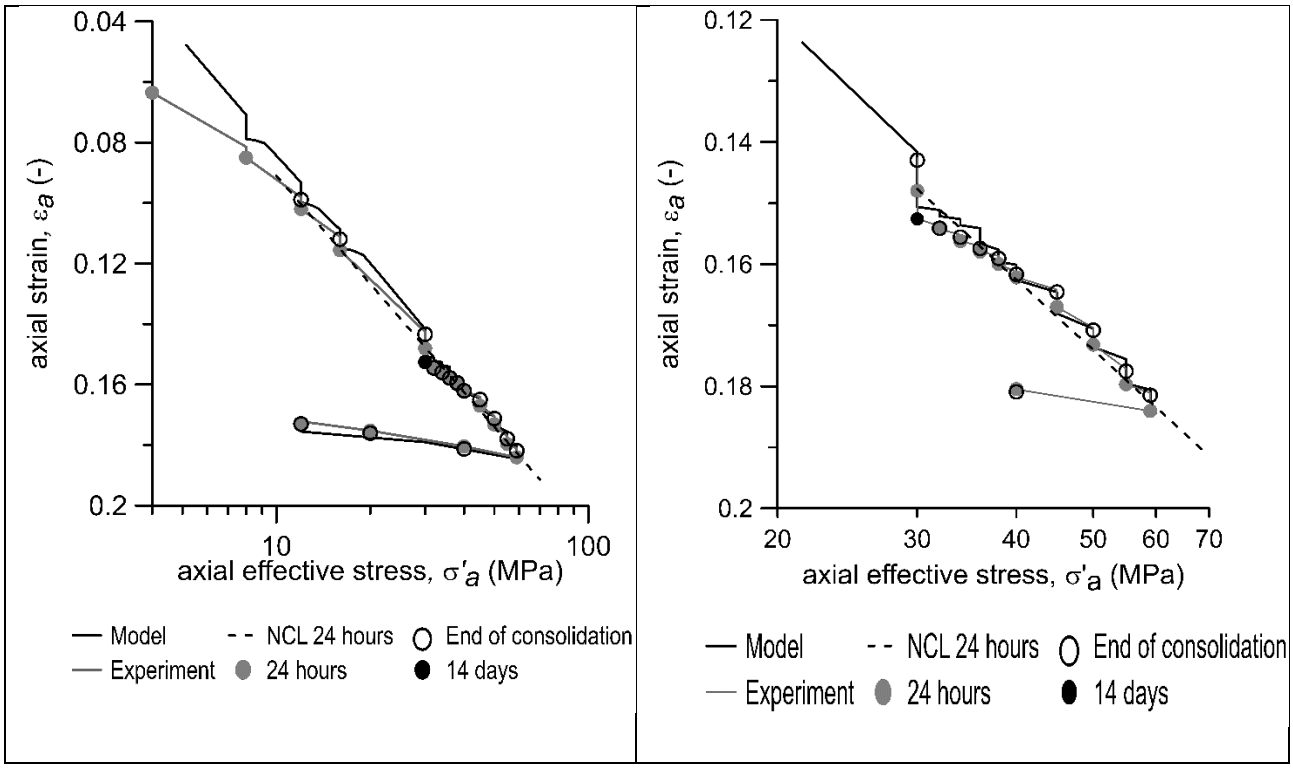

Fig. 6. LS2 test on coarse Field 2 sample. a) stress – strain curve, b) zoom on the hardening due to 14 days of creep

This effect can be further appreciated by observing the time history of the creep strains under different loads in Fig. 7a. σ'_a = 16 MPa and σ'_a = 30 MPa were both applied starting from a physical state which plots on the oedometer NCL, *i.e.* with $\frac{p'^d_c}{p'^r_c} = 1$ and consistently with eq (21) the strain rate developing under these loads is the same. However, because of the large strains accumulating during the 14 days of creep, the loads ranging from σ'_a = 32 MPa to 38 MPa are imparted from physical states on the left of the NCL, i.e. with $\frac{p'^d_c}{p'^r_c} < 1$. When these loads are applied the sample has then developed some apparent OCR, which, in light of eq. (21), justifies smaller strain rates. At higher stresses the experimental points plot on the NCL and the previous strain rate is obtained again when σ'_a = 55 MPa. Fig. 7b examines the effects on the creep strains of a loading - unloading – reloading sequence (LS3 test). Following a reloading step, such as under the σ'_a = 10 MPa imposed for 14 days in LS3, the creep strain rate is highly reduced. However, as a first loading condition is approached, the strain rates increases (σ'_a = 16 MPa) and it gets to a quite constant value at higher tress (σ'_a = 25 MPa and σ'_a = 40 MPa). It is interesting to note that the strain rate does not depend on the duration of the current creep phase, as in Fig. 7a the strain rates for 16 MPa, 30 MPa and 55 MPa are all the same, so that it can be concluded that a creep phase of 24 hours should be enough for a reliable characterization, provided that it is imparted from a condition such that $\frac{p'^d_c}{p'^r_c} = 1$.

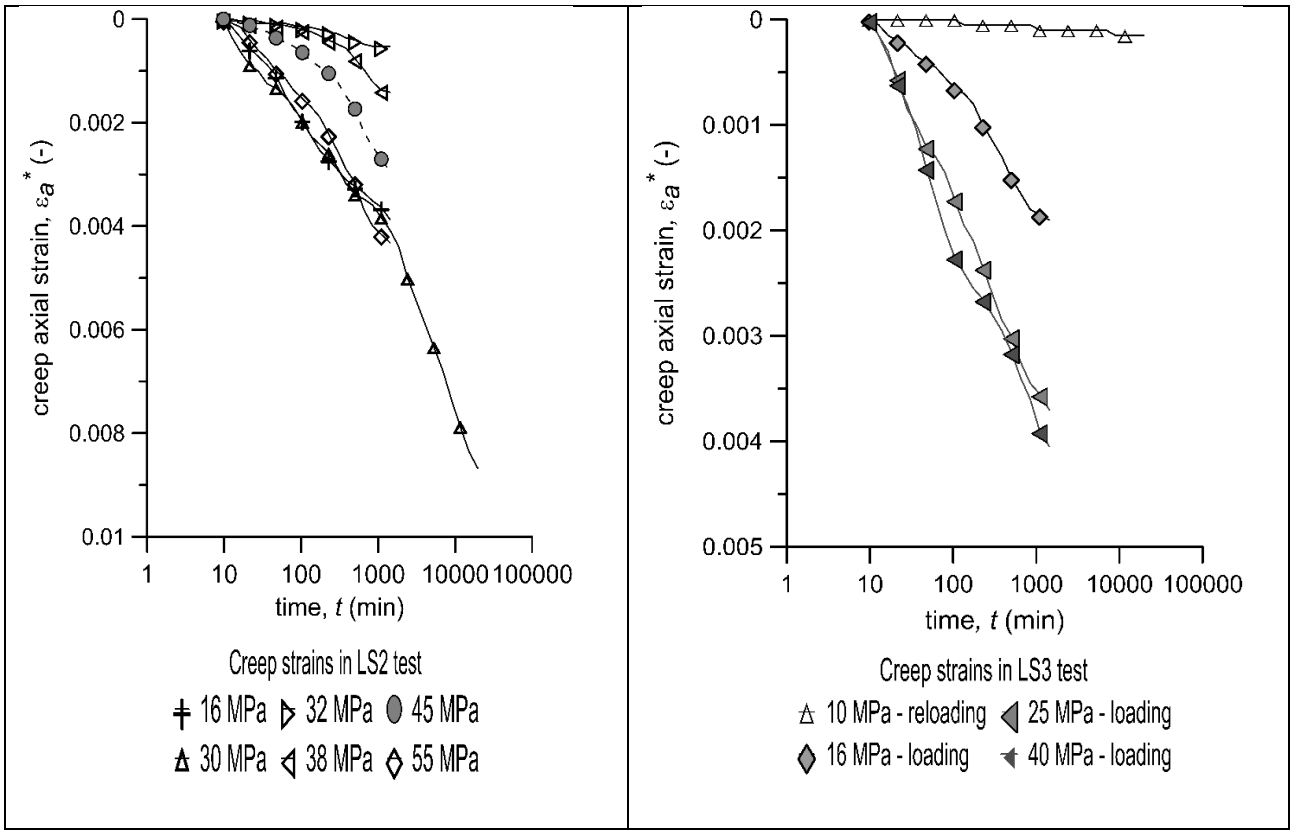

354 **Fig. 7.** Effect of history on strain rates. a) creep strains from a monotonous loading sequence, with a long creep at σ'_a =
355 30 MPa (LS2); b) creep strains from a loading – unloading – reloading sequence (LS3).

356 Model capabilities were also checked against conditions of imposed strain rate. Fig. 8 shows the strain history (a) and the
357 stress – strain relationship (b) for one of the CRS-K_0 tests on a Field 1 sample. The hardening effect of creep is well
358 evident both in the experiment and in the simulations, which prove to be adequate also for the different material and
359 testing conditions.

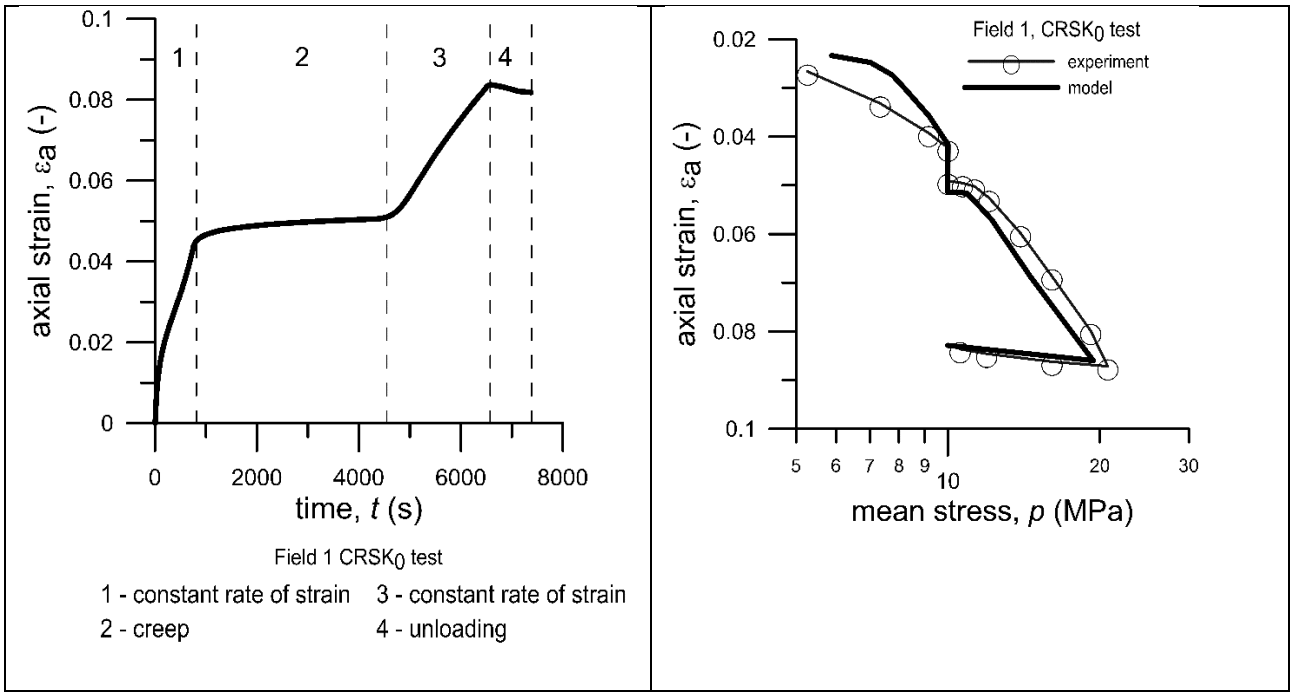

Fig. 8. CRS-K_0 test on Field 1 sample. (a): strain history. (b): stress - strain curve.

Table 2 provides the ranges of parameter values estimated from each test, which were also used in their simulations. As for the Field 1 case, no significant influence of testing procedure on parameters was found.

Table 2

Range of parameter values determined from the laboratory tests.

	λ^* (-)	κ^* (-)	μ^* (-)
Field 1 – step load oedometer	$6.1 \div 6.8\ 10^{-2}$	$0.5\ 10^{-2}$	$1.5 \div 1.7\ 10^{-3}$
Field 1 – CRS-K_0	$5.0 \div 6.8\ 10^{-2}$	$0.7 \div 1.1\ 10^{-2}$	$1.1 \div 1.5\ 10^{-3}$
Field 2 – coarse	$4.8 \div 7.6\ 10^{-2}$	$0.2 \div 0.8\ 10^{-2}$	$0.5 \div 1.3\ 10^{-3}$
Field 2 – fine	$6.8 \div 7.0\ 10^{-2}$	$1.1 \div 1.2\ 10^{-2}$	$1.4 \div 1.8\ 10^{-3}$

4. Case Histories

The experimental campaign and related numerical simulations suggested that the VNM can provide a quite good reproduction of the behaviour in oedometer conditions of reservoir samples from two gas fields. This section presents the results of the studies of the real field cases for the two fields, carried out through Finite Element simulations and adopting the VNM as described in section 2.3. As stated, the two fields are located in the northern and central portions of the

Adriatic Sea. In this area, gas reservoirs are generally constituted by alternances of sandy and shaly layers, deposited during the Pliocene and Pleistocene ages (Carola formation till Porto Garibaldi formation) that form multilayered systems in which every layer may have its own gas-water contact and a thickness variable from a metric scale to thin layers of few centimeters. The shaly layers are the source rocks of the biogenic gas while the trapping mechanism can be structural/mixed structural or stratigraphic type. Porosity of hydrocarbon bearing sandy layers is very variable, from very low values in thin beds environments up to more than 25% in conventional reservoirs. Gas from Adriatic Sea fields is generally withdrawn through several wells whose production is gathered toward one or more platforms per field. Most of these platforms are equipped with a continuous GPS station for the monitoring of subsidence evolution. In several fields, a well is equipped with radioactive markers for the measurements of the compaction of the reservoir rock in time[6,55,56]. The companies operating the gas fields are in charge of providing, and periodically updating, subsidence forecasts for each field based on detailed 3D numerical fluid-dynamic and mechanical models in order to demonstrate the environmental sustainability of their activities. The results of these models have to correctly reproduce the historical monitoring data acquired in the field: the two real cases presented in this section aim at highlighting the improvement in the accuracy of these studies achieved through the adoption of the VNM model, whose implementation in a FE code was previously tested against synthetic cases[57-58].

Herein, all subsidence values for each field were normalized with respect to the maximum subsidence obtained in the simulation performed with the VNM constitutive model at the GPS station location.

4.1 Workflow

First, a 3D geological model was built starting from reflection seismics and populated with petrophysical properties from well logs and laboratory analysis of core samples. Next, the geological model was converted into a Finite Difference fluid-dynamic model of the reservoir, that evaluates the time evolution of pore pressures in the whole computational domain. Pore pressure fields at selected time steps were finally provided, in a one-way coupled framework, to the 3D finite element geomechanical model, built using the commercial software Abaqus®.

To correctly evaluate the evolution of the stress state above and around the reservoir and, consequently, correctly predict the evolution of land subsidence, the geomechanical model also includes the rocks surrounding the reservoir, namely the overburden, underburden and sideburden regions. The reservoir rocks were described by means of appropriate elasto-plastic or elasto-viscoplastic constitutive laws (e.g. Modified Cam-Clay - MCCM - and VNM for the present cases, whose parameters were derived from the laboratory tests described in section 3), while the rocks surrounding the reservoir were considered as linear elastic. Appropriate stress-dependent rock compressibilities were used in the fluid-dynamic model to ensure consistency with the mechanical behaviour in the geomechanical model. Because of the non linear,

anelastic behaviour of the reservoir rock, the geomechanical predictions depend on the initial stress state, which must be identified adequately (see e.g. Refs. 59-60). Here it was determined as follows: the total vertical stress was obtained by integrating the bulk density profile versus depth, while the horizontal stress was obtained combining drilling information, stress tests and regional data when available. Boundary conditions imposed to the model prescribe null horizontal displacements of the lateral faces and no displacement in the three directions at the bottom face. Initial geostatic equilibrium is achieved by imposing the gravity force at the model elements. The simulations were then carried out allowing the model to evolve, following the time variation of pore pressure values derived from the fluid-dynamic simulation at each time step. Simulations were continued for 30 years after the end of production, in order to evaluate the effect of pore pressure equilibration after shut down.

While for elasto-plastic models like the MCCM, the initial position of the yield surface, determined by the parameter p'_c in eq. (2), only depends on the maximum stress ever experienced by the material, in the case of elasto-viscoplastic models like the VNM, the definition of the initial position of the reference yield surface, *i.e.* of p'^{r}_{c}, requires a more elaborated approach that also takes into consideration time and strain rates. In fact, the initial viscoplastic strain rate of the model must be consistent with the one of the material *in situ*, which in light of eq. (21) provides a constraint on the initial value of the $\left(\frac{p'^{d}_{c}}{p'^{r}_{c}}\right)$ ratio. For the Adriatic basin it is reasonable to assume a constant strain rate induced by the sedimentation process, given by:

$$\dot{\varepsilon}_v^{sed} = -\frac{\Delta e}{(1+e_0)\Delta t} \tag{22}$$

where e_0 is the void ratio at the beginning of sedimentation and Δt is the age of the sediments.The viscoplastic component of the sedimentation strain rate was obtained by subtracting the elastic component from the total one, i.e. as $\frac{\lambda^*-\kappa^*}{\lambda^*}\dot{\varepsilon}_v^{sed}$

The initial value of the apparent OCR, *i.e.* the $\left(\frac{p'^{r}_{c}}{p'^{d}_{c}}\right)$ ratio, can then be obtained by inverting eq. (21):

$$\mathrm{OCR} = \left(\frac{\lambda^*-\kappa^*}{\lambda^*}\frac{\tau}{\mu^*}\dot{\varepsilon}_v^{sed}\right)^{-\frac{\mu^*}{\lambda^*-\kappa^*}} \tag{23}$$

4.2 Field 1

Field-1 is an off-shore gas field located in the Adriatic Sea at about 20 km from the Italian coastline, with an average water depth of about 20 m. The reservoir is included in the Lower Pliocene sequences, situated from 1000 to 2200 mssl, characterized by an alternation of metric and plurimetric sandy, clayey and silty layers with variable proportions and thicknesses, classified as a proximal turbidite deposit in submarine fan facies. The field is bounded by a lateral facies variation toward north and east and by a NW-SE fault in the south west direction. Fourteen wells have been drilled in the

field and connected to the same production platform. A GPS station, located on the platform, was installed about 10 years after the start of production and has been recording data for more than 11 years.

The FE geomechanical grid of Field 1 consists of about 300,000 cells, resulting in more than one million degrees of freedom. Subsidence induced by production was simulated with alternative constitutive laws for reservoir rocks, *i.e.* elasto-plastic (MCCM) and elasto-viscoplastic (VNM). The simulation results were then compared to the vertical displacements recorded by the GPS station. As a first attempt, the λ and κ parameters for the MCCM introduced in the simulations were imposed as the mean values determined with all the laboratory tests on Field 1 samples (Table 2). For the eleven years of GPS recording, the MCCM predictions obtained following this approach ("MCCM_lab" in Fig. 9), are far from the GPS data. A further simulation was then performed with MCCM constitutive law, tuning λ and κ parameters (assuming different values in each geological layer) in order to better reproduce the GPS data: in this case the simulated evolution of subsidence ("MCCM" curve in Fig. 9) is much closer to the GPS series, but the subsidence trend is not correctly reproduced. The simulated curves show a slope change after about 7 years from the start of GPS recording (year 10 in the figure), which is not present in the GPS data. In both the MCCM models, the subsidence velocity increases because of a fast pressure drop due to a sharp increase in production rates, which however did not impact immediately on the recorded subsidence. This suggests that an elasto-plastic model may not be appropriate to describe the behaviour of the reservoir rocks, since it instantaneously responds to pressure changes, while the role of a viscous component cannot be neglected. The elasto-viscoplastic characterization of the reservoir rock enabled to better capture the subsidence history recorded by the GPS ("VNM" curve in Fig. 9). The VNM simulations were carried out using the mean values of λ^* and κ^* from the laboratory tests (Table 3), analogously to the first MCCM case, while only the creep index μ^* was calibrated within the admissible range from the experiments. The initial value of the apparent OCR was computed through the procedure described in section 4.1 and subsequently tuned on the basis of GPS data: the age of sediments was assumed equal to 3.8 millions of years according to previous sedimentological studies, the average value of the intercept of the NCL line determined from all oedometric tests (0.74) has been considered representative of the void ratio at the beginning of sedimentation and the current void ratio has been set equal to 0.3 according to current in situ porosity. Fig. 10 shows the modelled evolution of subsidence for the three cases, during the whole time-span from the start of production to the end of the simulation.

Table 3

Adopted mechanical parameters for "MCCM_lab" and calibrated "VNM" simulations of Field 1. All parameters are dimensionless.

λ	elasto-plastic compliance (“MCCM_lab” case)	$7.96 \cdot 10^{-2}$
κ	elastic compliance (“MCCM_lab” case)	$8.61 \cdot 10^{-3}$
κ^*	elastic compliance (strain)	$6.63 \cdot 10^{-3}$
ν	Poisson's ratio	0.3
λ^*	elasto-viscoplastic compliance	$6.13 \cdot 10^{-2}$
M	CSL slope	1.33
μ^*	creep index	$1.30 \cdot 10^{-3}$
OCR	apparent Over Consolidation Ratio	1.53

458

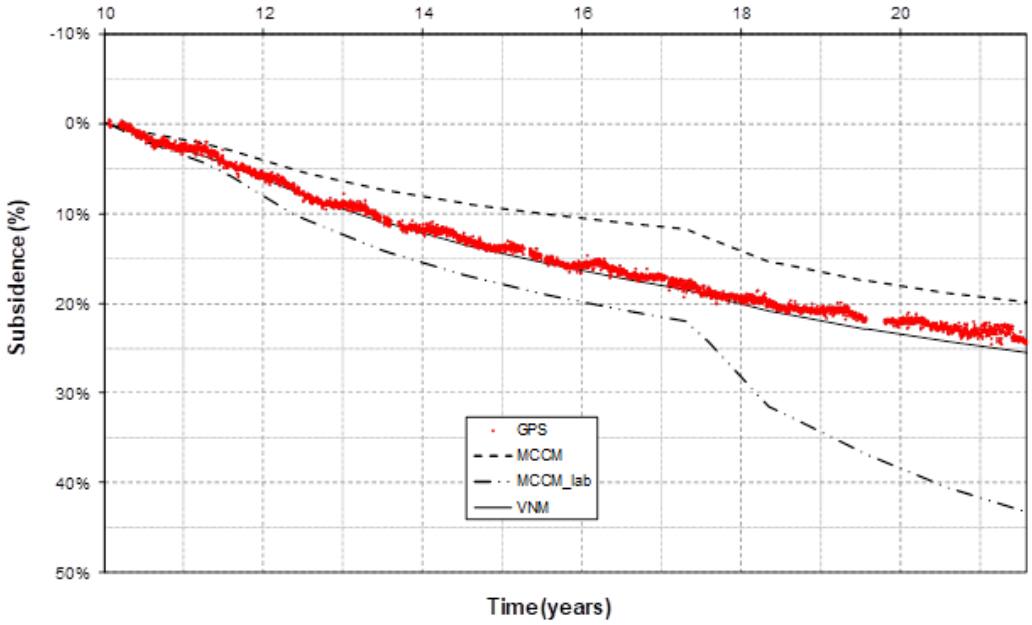

459

460 **Fig. 9.** Field 1: Comparison between evolution of measured and modelled vertical displacements from start of GPS recording

461

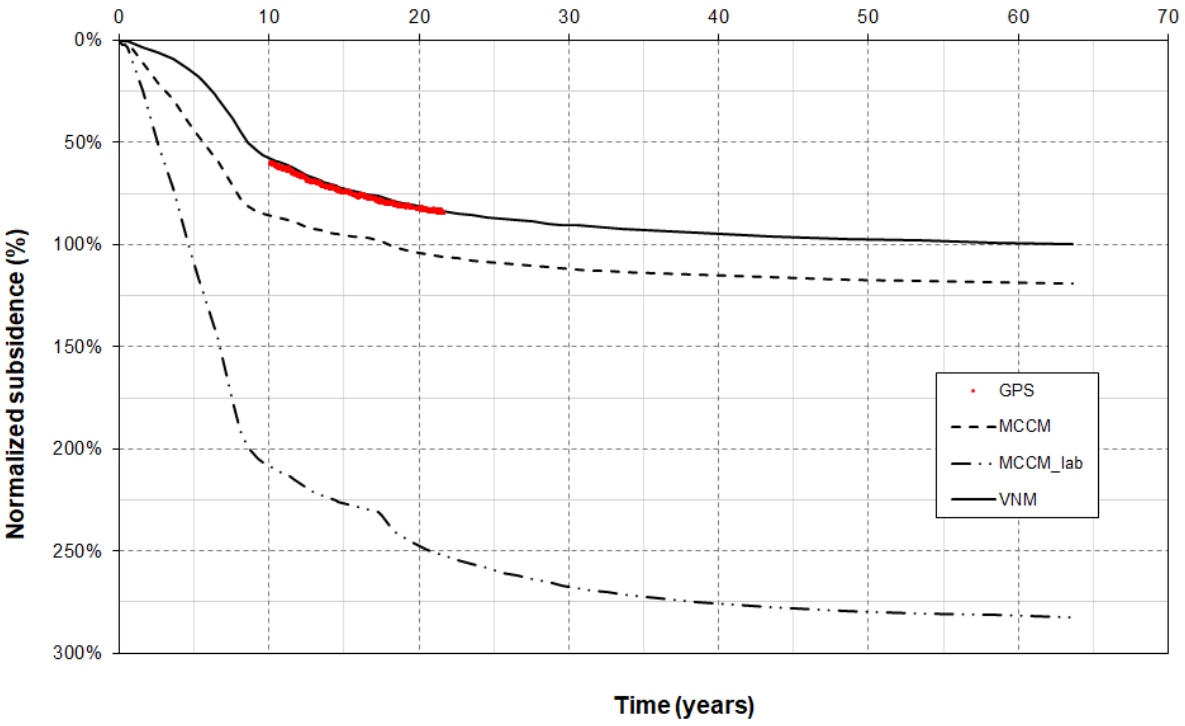

462

463 **Fig. 10.** Field 1: Evolution of modelled vertical displacement from the start of production to the end of the simulation, with
464 comparison with GPS series.

465

466 A bathymetric survey was carried out around 10 years after the start of production, *i.e.* approximately at the same time
467 when the platform was equipped with the GPS station. This survey allowed to build a map of the subsidence bowl, as the
468 difference between the assumed undisturbed sea bottom regional trend and the bathymetry measured by the survey. The
469 resulting map is shown in Fig. 11, together with the position of two sections of interest. In Fig. 11, the iso-subsidence
470 lines predicted with the VNM are overimposed to the measured ones.

471

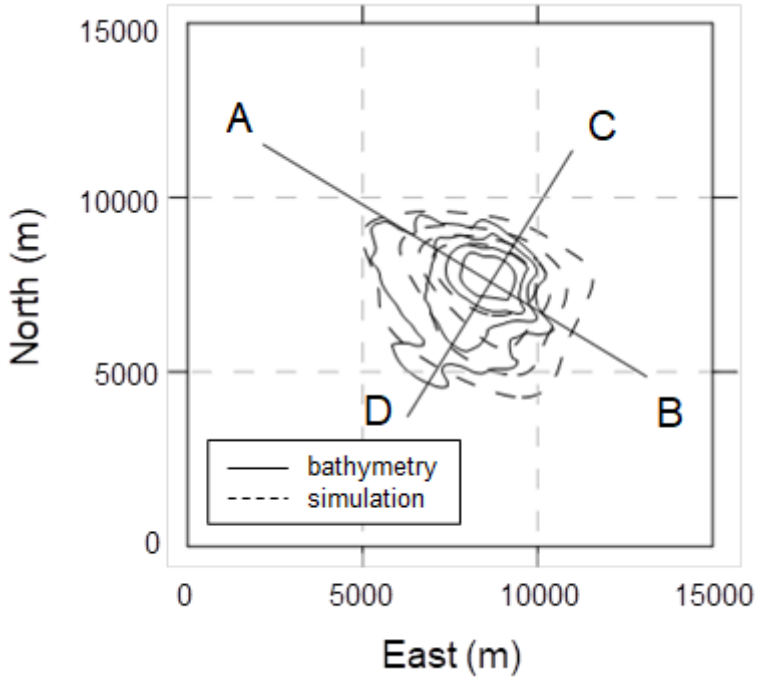

Fig. 11. Field 1: Subsidence from bathymetric survey and from model (contour lines 10%, 20%, 30%, 40%) and position of AB and CD sections.

A comparison between the results of the geomechanical studies and the subsidence after the first 10 years of production, as obtained from the bathymetric survey along the sections highligthed in Fig. 11, is shown in Fig. 12. Despite the fact that, for the following 11 years of GPS monitoring, subsidence is overestimated by the MCCM_lab simulation and it is slightly underestimated by the MCCM with GPS calibrated parameters (Fig. 9), at the time of the bathymetry the two elasto-plastic simulations are coherent in overestimating both the depth and extent of the subsidence bowl. Remarkably, the VNM simulation is able to accurately reproduce both the depth and the extent of the subsidence bowl directly using the laboratory derived parameters.

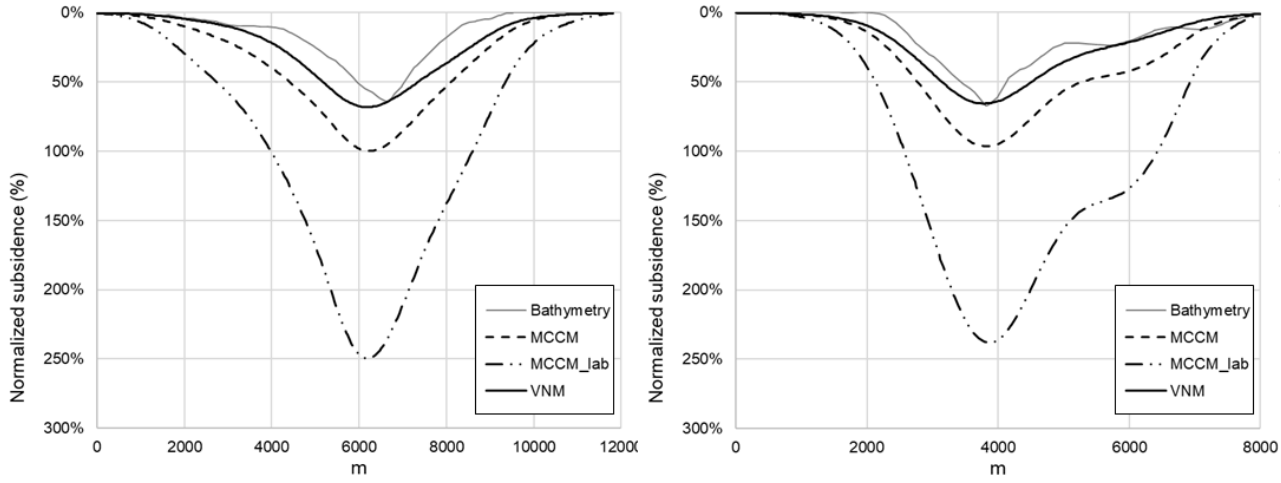

485 **Fig. 12.** Field 1: Subsidence from bathymetric survey and modelled subsidence along sections AB (a) and CD (b).

486

487 *4.3 Field 2*

488 This off-shore gas field is located in the Adriatic Sea, at about 60 km from the Italian coastline, where the average water
489 depth is around 60 m. Its structure is made up by an anticline with two culminations. The proximal turbiditic sand lobes
490 of the pleistocenic Carola Formation represent the shallowest and most recent reservoir layers, while the deepest reservoir
491 layers (pliocenic Porto Garibaldi Formation) are composed by distal turbidite sand lobes and fringes. These sandy
492 reservoir layers lie from 900 to 1800 mssl and gas is withdrawn by 28 wells, connected to platforms A and B. The two
493 platforms are equipped with GPS stations that have been acquiring data since the early production phases. GPS records
494 highlight a delay between gas production rate and vertical displacement rate variations, as shown in Fig. 13 for platform
495 B. One well of platform B has been equipped with markers for the monitoring of reservoir compaction and bathymetric
496 surveys have been performed before the start of production of Field 2 and after 7 years.
497 The simulation domain was extended to the North-East of Field 2 to include two nearby gas reservoirs that are potentially
498 interacting hydraulically and mechanically, thus resulting in an extent of the model of about 88 km x 73 km x 5 km. The
499 model was discretized with about $5.5 \cdot 10^5$ finite elements, for a total of around $2 \cdot 10^6$ degrees of freedom.
500 Initial simulations were performed with VNM material properties from average experimental values (tests described in
501 section 3), while the initial value of the apparent OCR was defined according to the procedure proposed in section 4.1
502 and by adopting the same hypoteses described for Field 1 case (age of sediments equal to 1.4 millions of years, void ratio
503 at the beginning of sedimentation equal to 0.63 and current void ratio equal to 0.28). Then, a tuning of the VNM
504 parameters allowed to accurately reproduce the GPS data recorded at platform B (Fig. 14). This step involved only minor
505 changes of the creep index μ^* (less than 4%) and of the apparent OCR (around 1%), while λ^* and κ^* were left unchanged
506 (see Table 4).
507 In Fig. 15 the results of the simulation performed with the VNM are compared to those obtained using the MCCM whose
508 parameters (λ and κ) are derived from laboratory experiments according to the well known expressions in section 2.3 and
509 reported in Table 4. The OCR of the MCCM simulation was set equal to the ratio between the maximum vertical stress
510 reasonably compatible with the tectonical and sedimentological history of the area and the current stress (OCR = 1.20) as
511 higher values would not be justifiable. This comparison highlights that VNM is able to provide an excellent match of
512 monitoring data by directly using laboratory derived parameters and reasonable assumption on the consolidation state of
513 the material.
514 While GPS data from platform B were used to tune the VNM parameters, other available data (markers, bathymetry and
515 GPS on platform A) were used to validate the geomechanical model. To this purpose, Fig.s 16 and 17 show comparisons

of model results in terms of reservoir compaction from markers and iso-subsidence lines from bathymetries, respectively. In particular, Fig. 16 shows the good agreement between cumulative compaction observed at the monitoring well and the VNM model estimates. All the measurements are reproduced within the confidence interval (+/- 3 standard deviation) or slightly overestimated, except for the measure acquired at year 11.7, which is out of trend and might be affected by acquisition uncertainties. The subsidence developed in the 7 years between the two bathymetric surveys is well reproduced by the model results (Fig. 17). Even if calibrated on data from platform B, the model properly reproduces also the subsidence rate recorded at the GPS station installed on platform A (Fig. 18).

Finally, Fig. 19 shows the time evolution of the 2 cm iso-subsidence line, the minimum distance from the coastline and the maximum extent at simulation-end, which is set 30 years after the production-end. It is apparent that the extent of the subsidence bowl after end of production tends to stabilize with time, expecially in the direction of the coastline.

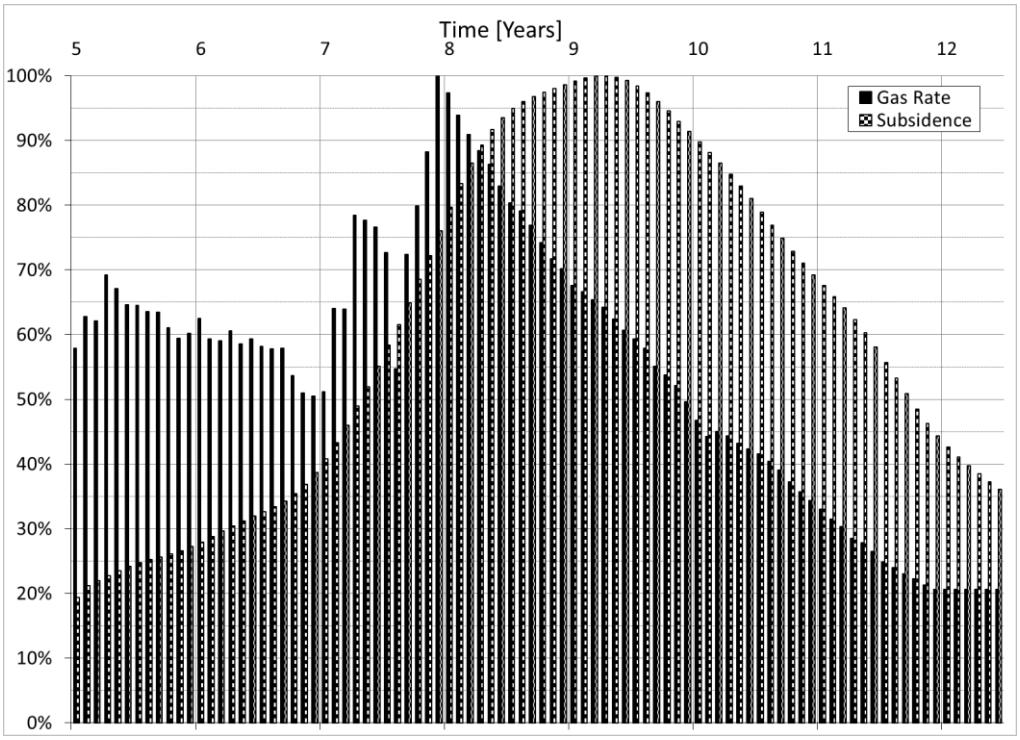

Fig. 13. Monthly data for platform B: gas production rate (black bars) versus subsidence GPS rate filtered from seasonal components (black and white bars).

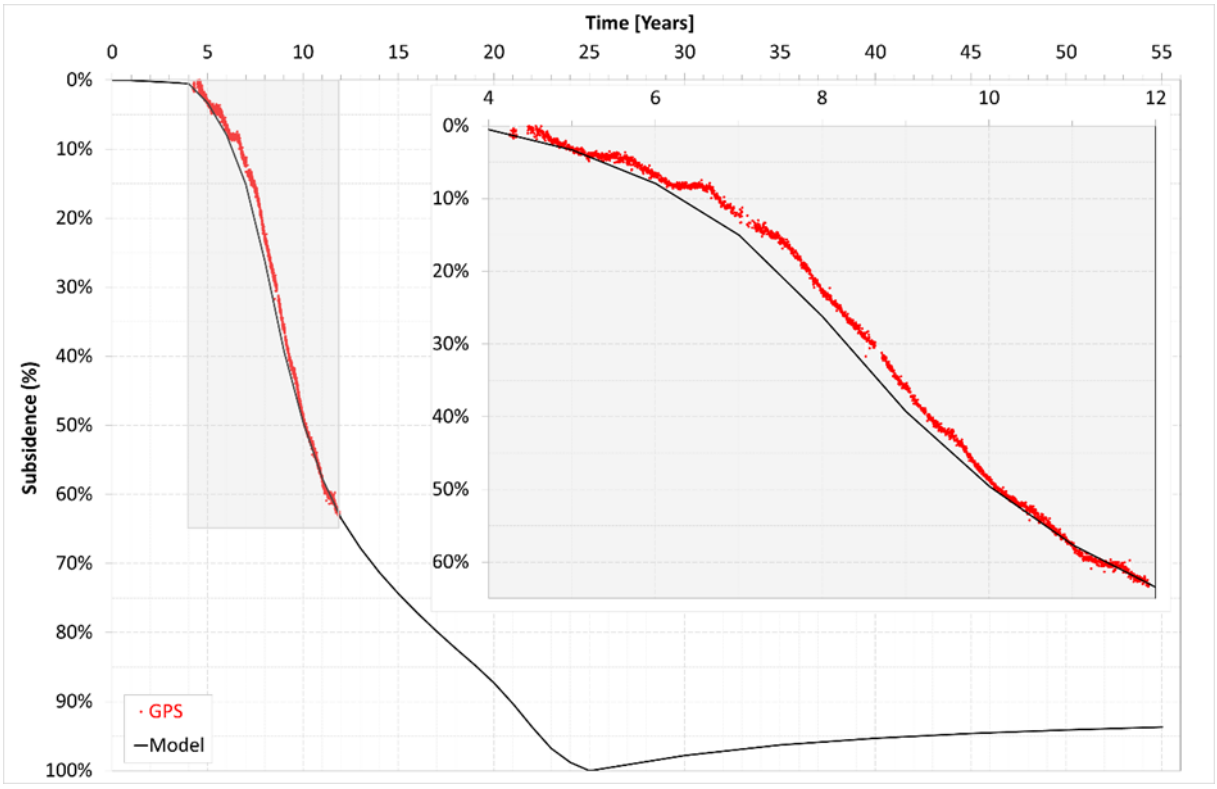

Fig. 14. Time evolution of subsidence at platform B (Field 2): GPS data versus model estimate, with magnification.

Table 4

Adopted mechanical parameters for "MCCM" and calibrated "VNM" simulations of Field 2. All parameters are dimensionless.

λ	elasto-plastic compliance	$7.76 \cdot 10^{-2}$
κ	elastic compliance	$8.40 \cdot 10^{-3}$
κ^*	elastic compliance (strain)	$6.19 \cdot 10^{-3}$
ν	Poisson's ratio	0.3
λ^*	elasto-viscoplastic compliance	$5.75 \cdot 10^{-2}$
M	CSL slope	1.33
μ^*	creep index	$1.06 \cdot 10^{-3}$
OCR	apparent-OCR	1.34

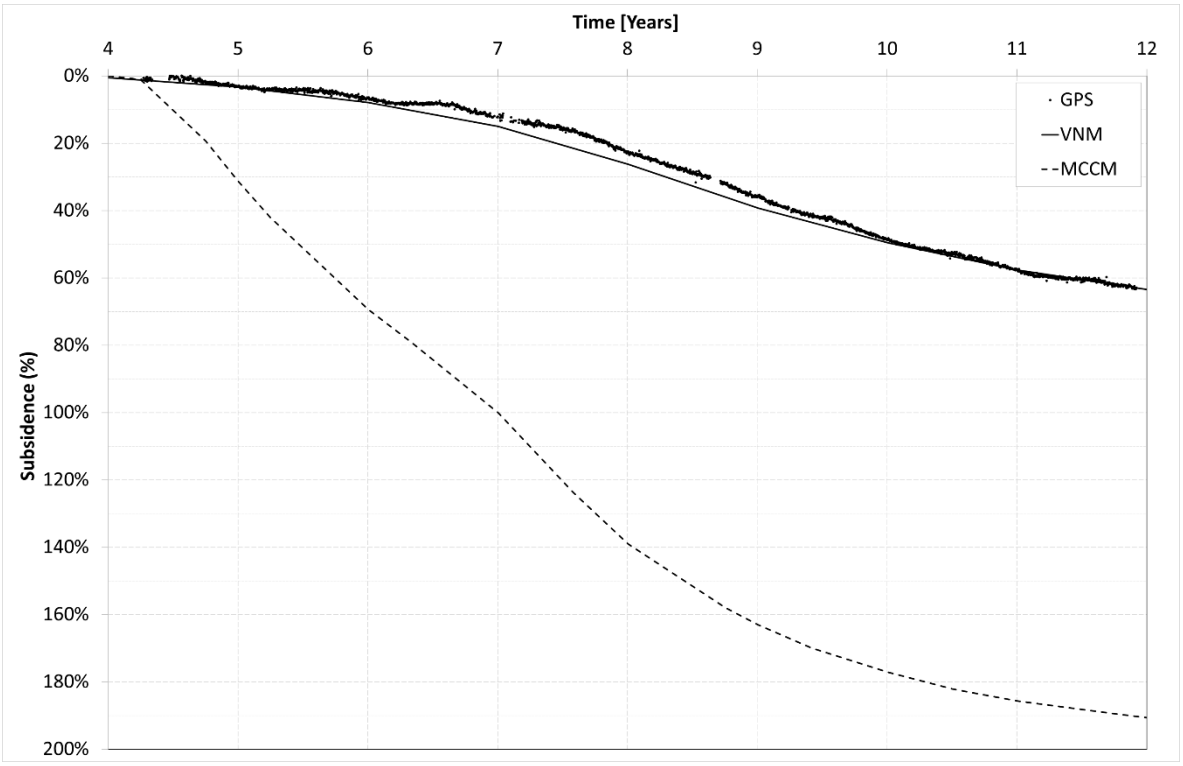

539

540 **Fig. 15.** Field 2: Comparison between evolution of measured and modelled vertical displacement in the period of GPS

541 recording.

542

543

544

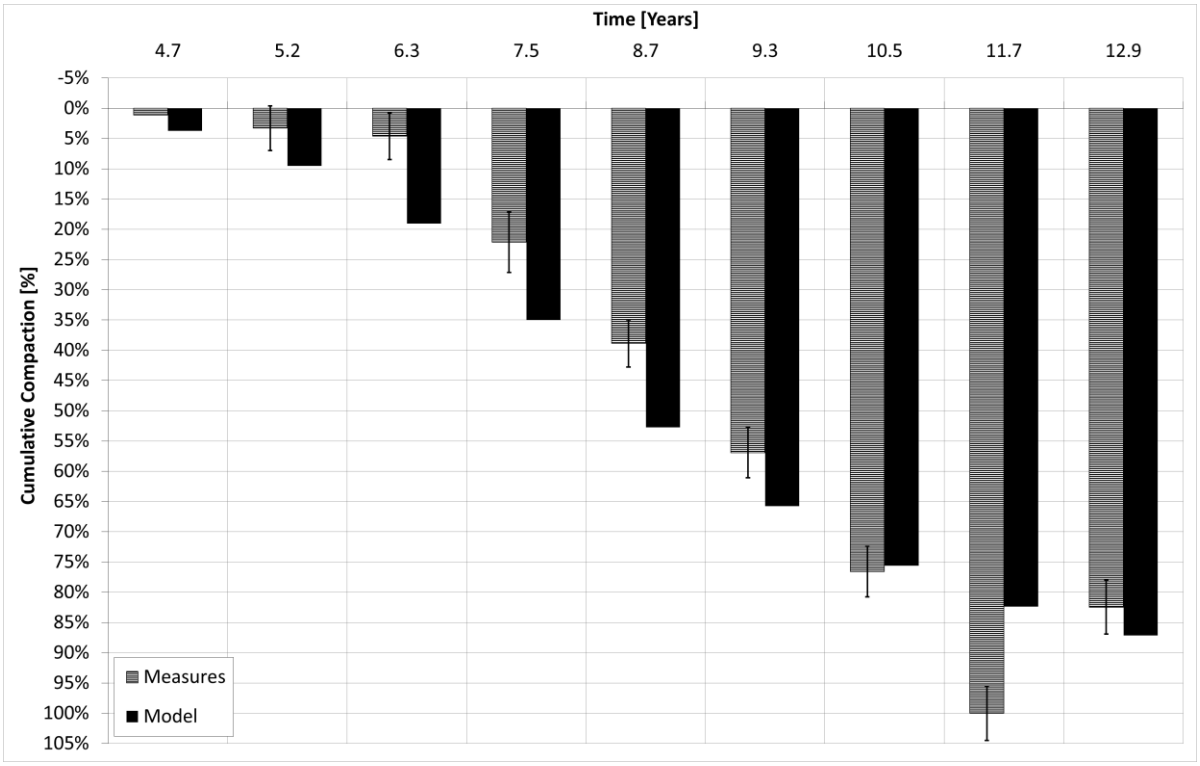

Fig. 16. Time evolution of compaction along the monitoring well of platform B (Field 2): markers data versus model estimates.

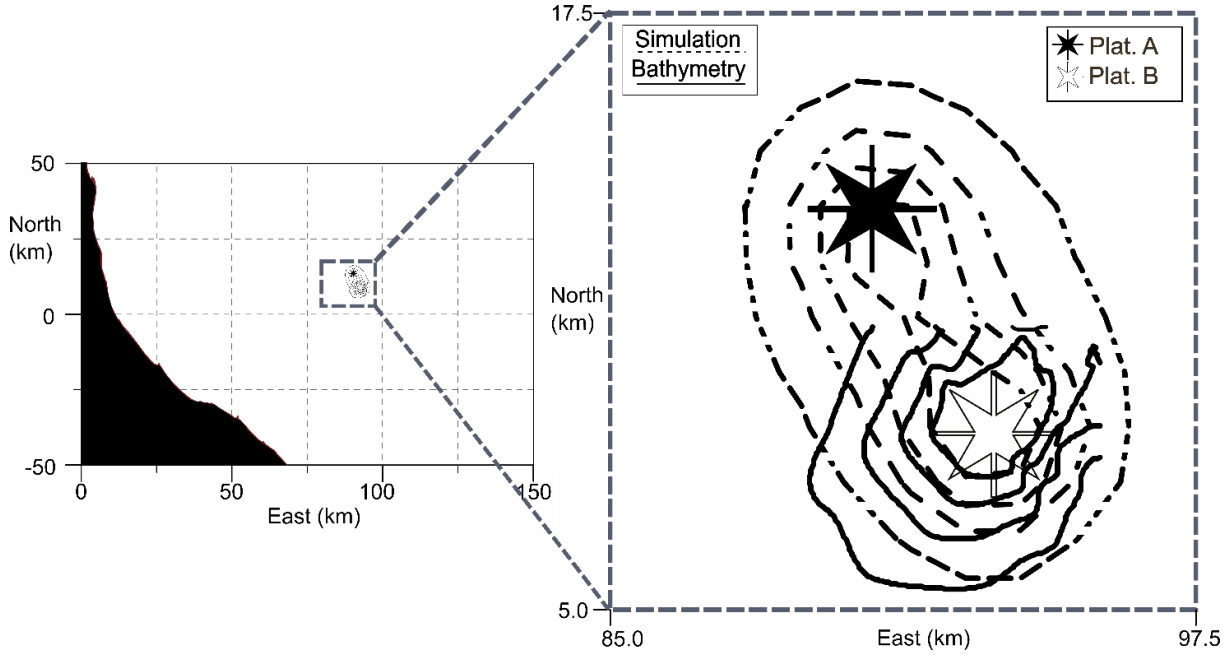

Fig. 17. Field 2: Contour lines (10%, 20%, 30% and 40%) of subsidence developed during the 7-year time interval between the two bathymetric surveys: model estimates (dotted lines) versus measured data (solid lines).

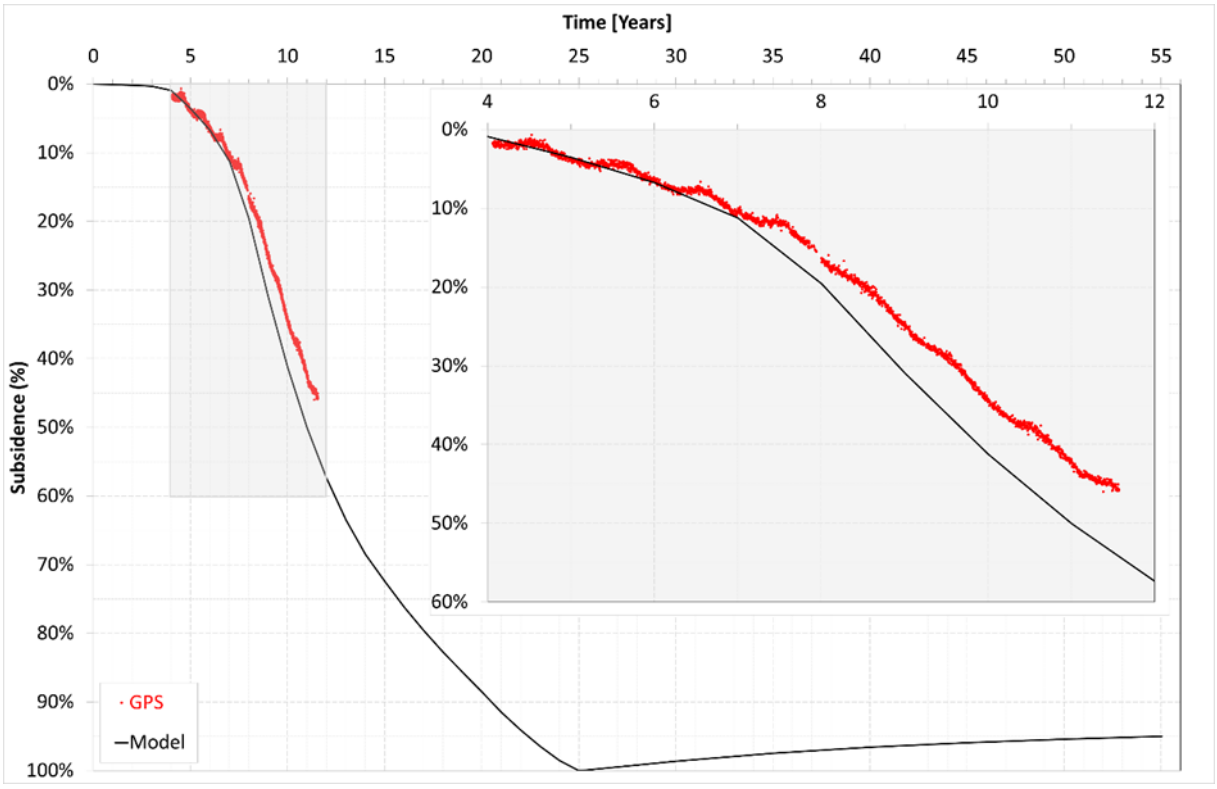

Fig. 18. Time evolution of subsidence at platform A: GPS data versus model estimate, with magnification.

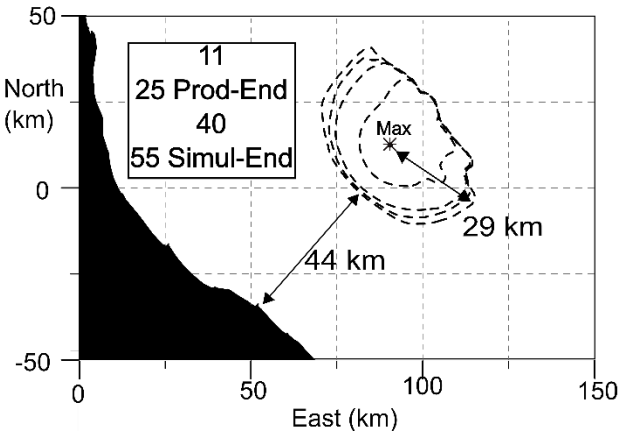

Fig. 19. Map with time evolution (after 11, 25, 40 and 55 years from start of production) of subsidence bowl extent. At simulation end (30 years after the production-end), the subsidence bowl gets minimum distance from coastline and maximum areal extent.

5. Conclusions

The evaluation and prediction of subsidence induced by hydrocarbon production is a complex task that involves advanced monitoring and modeling techniques. The long time series of monitoring data currently available highlighted that, in many cases, subsidence does not respond istantaneously to variations of fluids production rates. This 'delay' in subsidence response could be captured by adopting 'time dependent' models to describe the mechanical behaviour of the geological materials. Elasto-viscoplastic laws in the frame of the Overstress Theory offer a good compromise between simplicity and accuracy when modeling time dependent behaviour. Among them, the Vermeer Neher model is of particular interest, since model parameters can be derived from standard laboratory tests. The model was exploited to simulate the results of laboratory tests done on samples of reservoir sands and silts from two gas reservoirs from the Adriatic Basin. It adequately reproduced the main experimental outcomes, such as the dependency of the creep strain rates on the apparent OCR and the reduced compressibility upon loading after creep. At regional scale, Finite Element simulations of the subsidence of the two considered fields were also run using the VNM. A very good match of the monitoring data was obtained, both in terms of maximum subsidence value and areal extent. Interestingly, this was achieved using the compliance and creep parameters directly determined in the laboratory, while the apparent OCR was defined to be consistent with the geological history of the basin.

Acknowledgements

The authors gratefully thank Eni S.p.A. for the authorization to publish this work

References

1. Dixon TH, Amelung F, Ferretti A, Novali F, Rocca F, Dokka R, et al.. Space geodesy: Subsidence and flooding in New Orleans. *Nature*. 2006; 441(7093): 587–588.
2. Chan FKS, Mitchell G, Adekola O, McDonald A. Flood risk in Asia's urban mega-deltas: Drivers, impacts and response. *Environment and Urbanization ASIA.* 2012; 3(1): 41–61.
3. Dijkema K. Impact Prognosis for Salt Marshes from Subsidence by Gas Extraction in the Wadden Sea. *Journal of Coastal Research*. 1997; 13, 4: 1294-1304.
4. Murria J. Subsidence Due to Oil Production in Western Venezuela: Engineering Problems and Solutions. In *Land Subsidence (Proceedings of the Fourth International Symposium on Land Subsidence, May 1991)*. 1991. IAHS Publ. no. 200:129-140.

5. Takagi H, Fujii D, Esteban M, Yi X. Effectiveness and Limitation of Coastal Dykes in Jakarta: The Need for Prioritizing Actions against Land Subsidence. *Sustainability*. 2017; 9, 619.
6. Doornhof D, Kristiansen TG, Nagel NB, Pattilo PD, Sayers C. Compaction and Subsidence. *Oilfield Review*, Autumn 2006; 50-68.
7. Sulak RM. Ekofisk field: the first 20 years. *J. of Petroleum Technology, SPE, 43(10)*. 1991; SPE Paper SPE-20773-PA.
8. Fjaer E, Holt RM, Raaen AM, Risnes R, Horsrud P. *Petroleum related rock mechanics*. 2nd ed. Development in Petroleum Science, Vol. 53. Amsterdam, Holland: Elsevier; 2008.
9. Kim J, Tchelepi HA, Juanes R. Stability, Accuracy, and Efficiency of Sequential Methods for Coupled Flow and Geomechanics. Paper SPE-119084-PA. 2009.
10. Geertsma J. Problems of rock mechanics in Petroleum Production Engineering. *Proceedings of the First Congress of the International Society of Rock Mechanics*. 1966; 585-584
11. Geertsma J. Land Subsidence Above Compacting Oil and Gas Reservoirs. *Journal of Petroleum Technology*. 1973; 25: 06.
12. Mehrabian A, Abousleiman N. Geertsma's subsidence solution extended to layered stratigraphy. *Journal of Petroleum Science and Engineering*. 2015; 130: 68-76.
13. Tempone P, Fjær E, Landrø M. Improved solution of displacements due to a compacting reservoir over a rigid basement. Applied Mathematical Modelling. 2010; 34: 3352- 3362.
14. Roscoe K, Burland JB. On the generalized stress-strain behaviour of wet clay. *Engineering Plasticity*. 1968. Cambridge Univ. Press, 535-609
15. Abdulraheem A, Zaman M, Roegiers JC. A finite-element model for Ekofisk field subsidence. *Journal of Petroleum Science and Engineering* 1994; 10 (4); 299-310.
16. Capasso G, Mantica S. Numerical simulation of compaction and subsidence using Abaqus. *Proc. Abaqus Users' Conference*, Boston (USA). 2006: 125-144.
17. Gemelli F, Monaco S, Mantica S. Modelling methodology for the analysis of subsidence induced by exploitation of gas fields. *Proc. Second EAGE Workshop on Geomechanics and Energy, Celle (Germany)*. 2015.. cp-466-00001.
18. van Thienen-Visser K, Breunese JN, Muntendam-Bos AG. Subsidence due to gas production in the Wadden Sea: How to ensure no harm will be done to nature. *49th US Rock Mechanics / Geomechanics Symposium held in San Francisco*, CA, USA, 28 June-1 July 2015.

19. Morton RA, Bernier JC. Recent subsidence-rate reductions in the Mississippi Delta and their geological implications. *Journal of Coastal Research.* 2010; 26, 3: 555–561.
20. Chang C, Mallman E, Zoback M. Time-dependent subsidence associated with drainage induced compaction in Gulf of Mexico shales bounding a severely depleted gas reservoir. *AAPG Bulletin*. 2014; 98, 6: 1145–1159
21. Gemelli F, Corradi A, Volonté G, Mantica S, De Simoni M. Elasto-viscoplastic modeling of subsidence above gas fields in the Adriatic Sea. *Proceedings of the International Association of Hydrological Sciences*. 2020; 382:463.
22. Mossop A. An explanation for anomalous time dependent subsidence. *46th U.S. Rock Mechanics/Geomechanics Symposium, 24-27 June, Chicago, Illinois* 2012. Paper ARMA 2012-518
23. Hettema M, Papamichos E, Schutjens PMTM. Subsidence delay: field observations and analysis. *Oil & Gas Science and Technology*. 2002; 57(5): 443-458
24. Mesri G. Coefficient of secondary compression. J. *Soil Mech. Found. Div*., *ASCE*. 1973; 99 (1): 123-137.
25. Mesri G, Godlewski PM. Time and stress-compressibility interrelationship. *J. Geotech. Eng.* 1977; 103(5): 417-430.
26. Hagin PN, Zoback MD. Viscous deformation of unconsolidated sands – Part 1: Time-dependent deformation, frequency dispersion, and attenuation. *Geophysics.* 2004; 69, 3: 732-741.
27. Chang C, Zoback MD. Viscous creep in room-dried unconsolidated Gulf of Mexico shale (I): Experimental results. *Journal of Petroleum Science and Engineering*. 2009; 69: 239-246
28. Voyiadjis G Y, Zhou Y. Time-dependent modeling of subsidence due to drainage in bounding shales: Application to a depleted gas field in Louisiana. *Journal of Petroleum Science and Engineering*. 2018; 166: 175-187.
29. Vermeer PA, Neher HP. A soft soil model that accounts for creep. In *Proc. Int. Symp. "Beyond 2000 in Computational Geotechnics"*. 1999; 249-261, Balkema, Rotterdam.
30. Liingaard M, Augustesen A, Lade PV. Characterization of models for time-dependent behavior of soils. *Int. Journal of Geomechanics*. 2004; 4, 2: 157–177.
31. Naghdi PM, Murch SA. On the mechanical behavior of viscoelastic/plastic solids. *J. Appl. Meteorol*. 1963; 30: 321–328.
32. Olszak W, Perzyna P. Stationary and nonstationary viscoplasticity. 1970. McGraw-Hill, New York.
33. Šuklje L. The analysis of the consolidation process by the isotache method. *In: Proc. 4th Int. Conf. on Soil Mech. and Found. Engng., London.* 1957; 1:200–6.

34. De Gennaro V, Pereira JM. A viscoplastic constitutive model for unsaturated geomaterials. *Computer and Geotechnics*. 2013; 54:143–51.
35. Leroueil S, Kabbaj M, Tavenas F, Bouchard R. Stress strain-strain rate relation for the compressibility of sensitive natural clays. *Géotechnique.* 1985; 35 (2): 159–180.
36. de Waal J, Smits R. Prediction of reservoir compaction and surface subsidence: field application of a new model. *SPE Form Eval.* 198; 83:347–56.
37. Cassiani G, Brovelli A, Hueckel T. A strain-rate-dependent modified Cam-Clay model for the simulation of soil/rock compaction. *Geomechanics for Energy and the Environment* 2017; 11:42-51.
38. Qiao Y, Ferrari A, Laloui L, Ding W. Nonstationary flow surface theory for modeling the viscoplastic behaviors of soils. *Computers and Geotechnics*. 2016; 76: 105-119.
39. Alonso EE, Gens A, Josa A. A constitutive model for partially saturated soils. *Géotechnique* 1990; 40(3):405–30.
40. Malvern LE. The propagation of longitudinal waves of plastic deformation in a bar of metal exhibiting a strain rate effect. *J. Appl. Mech.*. 1951; 18: 203–208.
41. Perzyna P. The constitutive equations for rate sensitive plastic materials. *Q. Appl. Math.* 1963; 20, 4: 321–332.
42. Perzyna P. Fundamental problems in viscoplasticity. *Advances in Applied Mechanics.* 1966; 9: 243–377.
43. Yin Z-Y, Chang CS, Karstunen M, Hicher PY. An anisotropic elastic–viscoplastic model for soft clays. *International Journal of Solids and Structures*. 2010; 47, 5: 665-677.
44. Kutter BL, Sathialingam N. Elastic–viscoplastic modelling of the ratedependent behaviour of clays. *Géotechnique.* 1992; 42 (3): 427–441.
45. Yin JH, Zhu JG, Graham J. A new elastic–viscoplastic model for time dependent behaviour of normally and overconsolidated clays: theory and verification. *Canadian Geotechnical Journal.* 2002; 39 (1): 157–173.
46. Hickman RJ, Gutierrez MS. Formulation of a three dimensional rate dependent constitutive model for chalk and porous rocks. *Int. J. of Numerical and Anal. Meth. in Geomechanics*. 2006; 31 (4): 583-605.
47. Leoni M, Karstunen M, Vermeer PA. Anisotropic creep model for soft soils. *Géotechnique*. 2008; 58 (3): 215–226.
48. Hueckel T, Cassiani G, Tao F, Pellegrino A, Fioravante V. Aging of oil/gas-bearing sediments, their compressibility and subsidence. *Journal of Geotechnical and Geoenvironmental Engineering*. 2001; 127, 11: 926 – 938.
49. Leonards GA, Altschaeffl AG. Compressibility of clay. *J. Soil Mech. and Found. Div., ASCE.* 1964; 90(5): 133–155.

50. Bjerrum L. Embankments on soft ground. *Proc. of ASCE Spec. Conf. on Performance of earth and earth supported structures* 1972; 2: 1–54.
51. Bjerrum L. Problems of soil mechanics and construction on soft clays. *8th International Congress of Soil Mechanics and Foundation Engineering* 1973; 3: 111–159.
52. Mesri G, Feng TW, Benak JM. Postdensification penetration resistance of clean sands. *J. Geotech. Engrg., ASCE*. 1990; 116(7): 1095–1115.
53. Schmertmann JH. The mechanical aging of soils. *J. Geotech. Engrg., ASCE*. 1991; 117(9): 1288–1330.
54. Brignoli M, Fanuel P, Holt RM, Kenter CJ. Effects on core quality of a bias stress applied during coring. *SPE/ISRM Eurock 98, Trondheim (Norway)*. 1998; SPE47262.
55. Pemper R, Fjell L, Gold R. Field examples with a new compaction monitoring instrument. *38th SPWLA Annual Logging Symposium, June 15-18, Houston, Texas.* 1997; SPWLA-1997-MM.
56. Macini P, Mesini E. Radioactive markers technique application to evaluate compaction in environmentally sensitive areas. *SPE international petroleum conference and exibition. February 10-12, Villahermosa, Mexico.* 2002*; SPE74411*.
57. Nguyen SK, Volonté G, Musso G, Brignoli M, Gemelli F, Mantica S. Implementation of an elasto-viscoplastic constitutive law in Abaqus/Standard for an improved characterization of rock materials. *Abaqus Users' Conference, Boston (USA), Natural Resources*. 2016; 710: 710–724.
58. Cremonesi M, Ghisi A, Perego U, Corradi A, Gemelli F, Mantica S. A Numerical Study on Explicit vs Implicit Time Integration of the Vermeer-Neher Constitutive Model. In: Carcaterra A, Paolone A, Graziani G, eds. *Proceedings of XXIV AIMETA Conference 2019*. AIMETA 2019.
59. Della Vecchia G, Pandolfi A, Musso G, Capasso G. An analytical expression for the determination of in situ stress state from borehole data accounting for breakout size. *International Journal of Rock Mechanics and Mining Sciences.* 2014; 66, 64-68, ISSN 1365-1609.
60. Scelsi G, De Bellis ML, Pandolfi A, Musso G, Della Vecchia G. A step-by-step analytical procedure to estimate the in-situ stress state from borehole data. *Journal of Petroleum Science and Engineering*. 2019; 176: 994-1007.